Investigation of Aeroacoustic Effects of Trailing-Edge Modifications to Blades of a Coaxial Counter-rotating Rotor

by

Karlyle Munz

A thesis submitted to the Graduate Faculty of
Auburn University
in partial fulfillment of the
requirements for the Degree of
Master of Science

Auburn, Alabama
December 12, 2020

Keywords: Rotorcraft, Drone, Acoustics, UAV, Aeroacoustics, Serrations

Approved by

Vrishank Raghav, Assistant Professor of Aerospace Engineering
Brian Thurow, Department Chair, Professor of Aerospace Engineering
David Scarborough, Assistant Professor of Aerospace Engineering

Abstract

Noise generated by the rotor blades of modern UAVs pose significant limitations to the widespread adoption of UAVs in the future. To mitigate noise production, rotor blades with a serrated trailing-edge have been used to reduce the overall sound pressure level (OASPL) generated by these systems. Past studies, primarily conducted for single rotor systems, have demonstrated moderate reductions in frequency specific sound pressure levels, and reductions as high as 3 dB in OASPL. However, the efficacy of such noise mitigation techniques for rotors operating in a coaxial configuration, a common design in modern UAVs, have yet to be studied. The primary objective of this study is to characterize the sound pressure level reduction capability of the addition of trailing-edge serrations on a coaxial counter-rotating rotor system. A counter-rotating coaxial rotor test stand was designed and fabricated to enable independent rotor thrust and torque measurements, while an array consisting of 8 microphones was used to map the acoustic field of the rotors in operation. The aerodynamic and aeroacoustic performance of the coaxial counter-rotating rotor system were evaluated with and without serrated trailing-edges. Results confirmed that serrations on the trailing-edge of the rotor blades of a coaxial rotor with a fixed pitch angle and rectangular planform area, attenuate OASPL by 0.9 dB collectively and the middle-to-high sound pressure level (MHSPL) by 1.8 dB. Twisted rotor blades with serration modifications displayed a benefit as high as 2.5 dB, with some combinations of rotational speed and azimuthal angles showing negative reductions. It is expected that increased turbulent mixing is responsible for the decrease in overall sound pressure level from the serrated blades. Particle image velocimetry was used to confirm the contribution of turbulence in the downwash. In summary, the modifications made to these coaxial rotors were found to be less beneficial to the overall noise produced by the system, when compared to a single rotor UAV.

Acknowledgments

I would like to express my appreciation for Dr. Vrishank Raghav and all members of the Applied Fluids Research Group for their support in the completion of this research. I would also like to thank Dr. David Scarborough and Dr. Brian Thurow for serving on my committee. In addition, I would like to thank Dr. Eldon Triggs for his advice in 3D printing techniques. Lastly, I would like to thank Mr. Andy Weldon for machining the components used in this study.

Table of Contents

List of Figures

List of Tables

List of Abbreviations

α	Twist Angle
μ	Mean of N trials
Ω	Rotational Speed
ϕ	Latitude Angle below Rotor Plane
σ	Standard Deviation
θ	Azimuth angle
AR	Aspect Ratio
b	Blade Span
c	Airfoil Chord Length
C_Q	Coefficient of Torque
C_T	Coefficient of Thrust
D	Rotor Diameter
f	Frequency
FM	Rotor Figure of Merit
MHSPL	Middle-to-High Sound Pressure Level
N	Number of Trials
n	Number of Blades

OASPL	Overall Sound Pressure Level
P	Pressure
PIV	Particle Image Velocimetry
Q	Shaft Torque
R	Rotor Radius
RC	Root Cut-out
SPL	Sound Pressure Level
T	Thrust
z	Axial Separation between Rotors

Chapter 1

Introduction

1.1 Motivation

Unmanned aerial vehicles (UAVs) have been in use since the early nineteen-hundreds for a variety of purposes, but they originated as a means for surveillance [1]. The prevalence of small UAVs has seen a great increase in the past decade. It is estimated that global militaries have, thus far, spent 20 billion dollars on small UAVs [2]. The modern uses of small UAVs range from far-field surveillance to the close proximity of parcel delivery. The fact that these vehicles are becoming so common makes the implications of small rotorcraft in urban environments of great concern to the designers and engineers involved. The use of these aircraft create a logistical challenge not only due to their aerodynamic control requirements but also because of their auditory signatures. When machinery such as these are operated in close proximity to humans it is important to take into account the effect that they have on human hearing. Unfortunately, for these small UAVs, the noise produced is especially noticeable due to the high frequency and long-term usage of such machinery to sustain steady flight. The requirements set out by the Occupational Safety and Health Administration state that no person should be exposed to sound levels greater than 90 dBA for longer than 8 hours with a 5 dBA exchange rate [3]. For both military and recreational applications, the noise produced by rotorcraft is a challenge that is often not addressed. However, the noise produced by rotorcraft, whether it be a single or coaxial rotor, has repercussions related to the health of bystanders, as well as the effectiveness of the rotorcraft in terms of stealth [4]. This issue is becoming increasingly important as full-sized coaxial rotorcraft are becoming more popular [5]. Therefore, there is a need to model and understand the noise sources from a small-scale coaxial rotor UAV.

1.2 Background

Acoustic evaluation is an integral step in the design of many mechanical systems. The addition of moving parts increases the potential for additional noise sources. The noise produced by a mechanical system is a result of the acoustic waves created by the vibration of these parts. The propagation of such waves is dependent on the medium through which it moves as well as the distance it travels. Equation 1.1 shows that the magnitude of the sound experienced by human ears is quantified as the root mean squared pressure, P_{rms} as well as a reference pressure, P_{ref}. The basis for the SPL equation can be expanded to form the overall sound pressure level, as shown in Equation 1.2. This OASPL accounts for the sound pressure fluctuations for the entire frequency range that was quantified. Beyond this, the middle-to-high sound pressure level, shown in Equation 1.3, can be quantified by changing the frequency bounds at which the integral is taken. MHSPL has been identified in a previous study to focus on a range of frequencies where certain rotor modifications can be especially beneficial [6].

$$SPL = 20 \times log\left(\frac{P_{rms}}{P_{ref}}\right); P_{ref} = 2 \times 10^{-5} Pa \tag{1.1}$$

$$OASPL = 10 \times log\left(\int_{20}^{20000} \frac{PSD(f)df}{P_{ref}^2}\right); \tag{1.2}$$

$$MHSPL = 10 \times log\left(\int_{4000}^{12800} \frac{PSD(f)df}{P_{ref}^2}\right); \tag{1.3}$$

Moving further beyond general acoustics, aeroacoustics is the study of noise generation due to fluid motion. Contributions to the field of aeroacoustics have led to substantial reductions in noise produced by mechanical systems such as jet turbine engines used in commercial aircraft [7]. In machinery such as turbine engines, that process large amounts of air at a very high rate, the causes of noise production are highly dominated by aeroacoustic noise sources [8]. Aeroacoustic principles similar to those used on jet turbine engines also apply to the noise generated by rotorcraft.

1.2.1 Sources of Rotor Noise

There are various sources that contribute to the acoustic signature produced by a rotorcraft. The imposition of the leading-edge as well as the convergence of the pressure and suction side air flows each provide unique opportunities for the generation of sound. In most theoretical estimations, three main types of noise sources are emphasized. The sources are listed below along with their connection to rotorcraft noise.

1. **Monopole Sound Source**: A monopole source is an omni-directional source that radiates acoustic energy equally in all directions. A monopole source can be modeled as a small pulsating sphere that expands and contracts sinusoidally [9]. The main source of monopole sound in a rotor system is thickness noise, which is associated with the displacement of air around a moving blade to accommodate its physical volume.

2. **Dipole Sound Source**: A dipole is formed by two monopoles of equal strength but opposite phase, that are separated by a small distance [9]. A dipole source does not radiate equally in all directions and has two maxima that occur at the halfway points between the separation points of the two monopoles. Dipole sounds are often produced by oscillating planar objects. In terms of rotorcraft, dipole noise is associated with loading noise, which is produced in proportion to the sectional loading on the blade. In this case the planar object is the rotor blade, and the oscillations are caused by trailing turbulence.

3. **Quadrupole Sound Source**: A quadrupole source is generated by two identical dipoles of opposite phase that are separated by a small distance. There is no net flux of fluid during the operation of a quadrupole source. Consequently, quadrupoles are poor radiators of sound [9]. Quadrupole noise is also produced by rotors and is most commonly caused by blade-vortex interaction.

In addition to the difference in the construction of these sources, they also display quantitative differences in directivity. These directivities are also altered depending on the phase of flight of the aircraft. For example, loading noise is more prevalent in cases of climbing maneuvers, and high speed impulsive noise is only present in forward or advancing flight [10]. The common directivities for each of these main noise sources are shown below in Figure 1.1.

Figure 1.1: Previously identified noise sources of a small UAV in forward flight [10]

Due to the various noise sources introduced by the operation of rotorcraft, multiple government agencies have taken interest in reducing this noise. The FAA specifically, has shown great interest in the recent past into the mitigation of aircraft and rotorcraft noise [11]. One of the initiatives in place is the CLEEN Project, which aims to reduce the noise emitted by civil aircraft by 32dB cumulatively. The ICAO (International Civil Aviation Organization) and CAEP (Committee on Aviation and Environmental Protection) have both agreed to this noise reduction standard [11]. While these regulations apply to full sized aircraft, the same noise related issues are becoming increasingly important in the world of remotely-piloted small-scale aircraft. In past studies it has been shown that alterations made to the shape of rotor blades can have a considerable effect on the acoustic signature of a blade and a rotor system as a whole. The main mechanism by which the noise of these modified rotors is thought to be reduced is by an increase in turbulent mixing. The focus of this study is to evaluate past efforts and contribute to the body of work that has developed with the end goal of reducing the acoustic signature of small UAVs.

1.2.2 Previous Methods of Attenuation

In past studies, multiple techniques that involve rotor design modification have been tested for their effectiveness as a noise attenuation method. Each of the methods mentioned here were evaluated for their past effectiveness and potential for future progress. The previous methods analyzed for their effectiveness are listed here:

1. **Number of Rotors/Blades**: In certain studies, the main objective has been aimed at reducing the loading or dipole noise of a rotor. Loading noise can be reduced in one of two ways. The first is by reducing the thrust produced by the rotor, however this approach would be counter-productive to the maneuverability of the aircraft. On the other hand, the thrust can be distributed across a higher number of blades, or more specifically, more rotors. An experimental study in the past has concluded that the noise produced by multirotor drones is altered by both the number and size of the rotors used [12]. More specifically, for a given thrust, the sound pressure for the first few harmonics has been shown to decrease with both increasing propeller diameter and increasing number of propellers (quadcopter, hexacopter, octocopter). This conclusion was reached through the use of an azimuthal array of 8 microphones and a power spectral density analysis in a study by Tinney and Sirohi. This increase in number of rotors for a given thrust resulted in a net reduction in OASPL [12].

2. **Duct/Absorptive Ducts**: Another method that has been studied for its aeroacoustic benefits on UAV rotors is the addition of solid ducts or absorptive ducts around rotors. Some ducts with high sound absorption coefficients were added to small rotors as a means of absorbing the tip noise caused by blade-vortex interaction [13]. Other ducts have been used to disrupt the vortices before they are formed. Unfortunately, the use of ducts have not provided substantial reductions in the OASPL of small UAV rotors, and can also reduce their aerodynamic performance [14].

3. **Tip Modifications**: Large drone manufacturers have already implemented tip modifications to reduce noise associated with trailing tip vortices. This is also the most currently prevalent method of sound attenuation being implemented on modern UAVs. These tip modifications have been proven to reduce the OASPL of UAV rotors by moderate margins. In a study by Van Treuren and Wisnewski, an SPL reduction of 7.2 dB was attained by modifying the tips of a DJI Phantom 2 rotor. However, this modification also led to an increase in power required by 4 percent [15].

4. **Leading-Edge Modifications**: Some bio-inspired leading-edge modifications have been found to be effective in reducing broadband noise in low turbulence inflow conditions. Leading-edge modification is another area that has been studied in great detail for the single rotor case. The general idea to implement leading edge modifications, especially serrations, came about as a result of bio inspired research [16]. Owl wings in particular have been studied in great detail in order to reveal the mechanism behind their ability to fly with a minimal acoustic signature. In a computational study by Rao, the leading edge of a rotor blade was modified to mimic the shape of the leading edge of an owl's wing. This study resulted in similar findings to the tip modification study. In this case, while the aerodynamic performance suffered, especially at low angles of attack, the high frequency SPL was consistently reduced. However, this trade off between aerodynamic and aeroacoustic performance is a challenge yet to be solved by these methods [16].

5. **Trailing-Edge Modifications**: Porous and solid trailing-edge modifications have been known to result in reduced high-frequency noise spectra. While this method may, at first glance, appear to predictably yield similar results to that of leading-edge modification, there are a few notable differences. The effectiveness of leading-edge serrations, unlike trailing-edge serrations, are highly dependent on the rotor's inflow conditions. In addition, rotors with the addition of trailing-edge serrations are able to reduce the OASPL of a spinning rotor, while doing so with negligible effects on the aerodynamic performance,

unlike leading-edge serrations [17]. Acoustic benefits and lack of change in aerodynamic performance have been observed most commonly in cases of low turbulence free streams of incoming velocity. This finding can be confirmed by an experimental forward flight study by Li, where the SPL was reduced by as much as 12 dB at higher frequencies. This finding was accompanied by a constant lift-to-drag ratio [17].

In another study by Yang et al. similar experiments were conducted by modifying the trailing edge of a single rotor blade with a serrated pattern [6]. In this forward flight study, it was found that the effectiveness of these serrations was dependent on their amplitude and frequency. Furthermore, it was found that the addition of serrations causes the most effective noise attenuation in a certain frequency range termed as the middle-to-high frequency range (4,000 to 12,800 Hertz), and denoted as MHSPL. In the process of analyzing frequency spectra for different blades with serrated trailing-edges, a critical value for the Strouhal number ($St = \frac{fL}{U}$) was discovered where no further noise reduction was observed. This number corresponds to $St_c < 30$ where St_c is the Strouhal number based on the airfoil chord length and the free-stream velocity. Flow field analyses showed that the introduction of sawtooth serrations promoted the formation of elongated coherent structures in the space between two consecutive teeth, together with hairpin vortices along the sawtooth edges [21].

In addition to aerodynamic and acoustic analyses, PIV measurements have been used to quantify the flow development around serrated and baseline single rotor blades [18]. In these studies, it was found that there are negligible differences in the mean flow around a baseline or serrated rotor at both hover and forward flight conditions and no difference in aerodynamic performance below a Reynolds number of 50,000. However, the wake shape and size of vortices passing the trailing edge was changed marginally. It was also hypothesized that this change in wake shape is responsible for an increase in flow mixing at the trailing edge.

Similar methods have been employed on wind turbine blades and fixed wing airfoils in the past [19]. Organic wings such as owls have been the inspiration for these trailing edge serrations. Owls are able to achieve near silent flight as a result of their wings due to a few characteristics. The first of these aspects is the soft downy coating on suction side of the wing surface. The next characteristic is the comb of stiff feathers at the wing leading edge. The third aspect is the feathers and wings with a fringe of flexible filaments [20]. Together, these characteristics lead to a wing that is able to achieve flight that is silent to human ears. It is thought that the implementation of trailing-edge serrations is effective as a noise reduction method due to destructive interference of the pressure fluctuations produced by the flow structures convecting along the slanted edge.

While there are benefits to the addition of serrations, the limitations of these serrations have also been studied. In a study by Ning is was observed that the tonal component seemed to increase in the low frequency region. Fortunately, at low velocities, serrations seemed to lead to greater noise reduction. There were three parameters considered in Ning's study. Firstly, the non-dimensional tooth height defined as the ratio between the tooth half-height and the boundary layer thickness $h^* = h/2d$. Secondly, the Aspect Ratio of the tooth defined as the ratio between the width and the half-height $AR_t = 2b/h$. Finally, the boundary layer thickness based Strouhal number $St_d = d/U$ [18].

Overall, trailing-edge serrations have proven to have potential as a viable solution to combat rotor noise. When implemented on a single rotor, trailing-edge serrations have proven to reduce the OASPL by 2-3 dB. These serrations have also reduced the frequency-specific SPL at the higher end of the human hearing spectrum, where noises appear louder. While the optimization of the sizes and proportions of these serrations has not been rigorously completed, multiple studies have narrowed the field of useful parameters for future studies. These blade modifications have shown benefits in the past and display potential for further research in the future.

The implementation of trailing-edge serrations was chosen as the main subject of the current study due to its ability to display moderate benefits in terms of acoustic performance, while performing most similarly to an unmodified blade in terms of aerodynamics. This combination of effects were the most promising in terms of reducing overall SPL while having minimal effects on the aerodynamic performance.

1.2.3 Mathematical Modeling of Rotorcraft Acoustics

Thus far, only experimental observations of the mitigation of rotor noise have been discussed. In the field of computational aeroacoustics there have been many attempts to completely, and in closed form describe the sound produced by a spinning rotor. The most prevalent and widely respected mathematical representation of rotor noise is the Ffowcs Williams-Hawkings (FW-H) Equation.

Beginning from the Navier-Stokes equation, the FW-H equation is used to describe how sound waves propagate when a fluid encounters a solid boundary such as a wing. The form of the Navier-Stokes equation used to develop the basic FW-H equation describes fluid momentum in two dimensions. In an intermediate step to the FW-H equation, Lighthill's Acoustic Analogy was developed to predict the pressure distribution in a fluid due to a solid jet in a quiescent medium. This acoustic analogy, shown in Equation 1.4, was used to map how stresses move through the fluid. The unfortunate drawback to Lighthill's Acoustic Analogy is that it is not accurate for transonic or supersonic flows.

$$\left[\frac{1}{c^2}\frac{\partial^2}{\partial t^2} - \nabla^2\right]^2 p' = \frac{1}{c^2}\frac{\partial^2 p'}{\partial t^2} - \nabla^2 p' = 0 \tag{1.4}$$

The final form of the Ffowcs-Williams Hawkings equation is shown below in Equation 1.5 as a two dimensional inhomogeneous equation used to describe the previously mentioned pressure field in terms of the Lighthill stress tensor.

$$\frac{1}{a^2}\frac{\partial^2(p')}{\partial t^2} - \frac{\partial^2(p')}{\partial x_i^2} = \frac{\partial}{\partial t}\left[\rho_a v_i \delta(f)\frac{\partial f}{\partial x_i}\right] - \nabla\left[\Delta p_{ij}\delta(f)\frac{\partial f}{\partial x_i}\right] + \frac{\partial^2 T_{ij}}{\partial x_i \partial x_i} \tag{1.5}$$

The right-hand side of the FW-H equation is divided into 3 distinct sections. These sections each represent a type of noise mentioned previously. The first is the monopole sound sources expressed as thickness noise, which are created by the direct displacement of fluid by the volume of the blade. Since the amount of fluid displaced between the baseline and serrated cases will not be changed, it is expected that the thickness noise term will not be affected in this study. The second section is the loading noise, also known as the main source of dipole noise in a rotor system. This loading noise is proportional to the thrust produced by the system. If the thrust produced by the rotor is not significantly altered, then it is not expected for this term to change. However, the magnitude of this loading term is highly dependent on the components of the generalized stress tensor p_{ij}. Therefore, the addition of serrated trailing edges could have an effect as the interaction between the pressure and suction sides of the rotor blade will be altered. The first two sections shown here are both dependent on the function of the blade surface f leading to a dependency on trailing edge profile.

$$T_{ij} = \rho u_i u_j + p_{ij} - c_0^2(\rho - \rho_0)\delta_{ij} \tag{1.6}$$

The last section of the equation accounts for the quadrupole sources of sound, namely the blade vortex interaction noise. This element interacts with the Lighthill stress tensor term T_{ij} shown in Equation 1.6. This term is responsible for broadband noise generation due to blade vortex interaction, which is known to be especially prevalent in coaxial counter-rotating rotors. While, the FW-H equation has been used as an extrapolation of the Reynolds-averaged Navier-Stokes (RANS) for serrated rotors, there are other models for sound approximation that have been developed specifically for rotors with serrated trailing-edges [22].

1.2.4 Mathematical Model of Serrated Rotor Blade Acoustics

A study in 1991 concluded that based on an asymptotic theory, serrations on the trailing-edge of a wing can result in significant noise reduction [23]. This was followed by the condition that the reduction is only present for a very high frequency range. Specifically, Howe's rule is useful for $\frac{\omega h}{U} >> 1$, with ω representing the rotational frequency, h representing the height of the serrations, and U, the inflow velocity. The limitations of this method also include that the length of the serration should be of the same order as the turbulent boundary layer δ. This rule was developed for both sawtooth and sinusoidal serrations. For a single serration length, the theory predicts larger noise attenuation for a sawtooth serration in all cases.

Howe's rule for sawtooth and sinusoidal serrations on the trailing-edge of a rotor blade as well as the estimations for the twisted blades in this study are shown in Equations 1.7 and 1.8. The variables λ and h are defined in Figure 1.2.

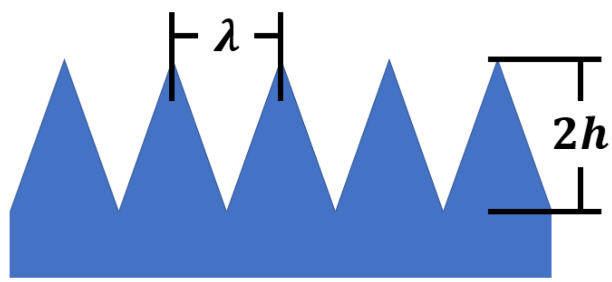

Figure 1.2: Definition of serration dimensions

$$\Delta SPL_{sawtooth} = 10 \times log \left[1 + \left(\frac{4h}{\lambda}\right)^2\right] = 12.3 \ dB \tag{1.7}$$

$$\Delta SPL_{sinusoid} = 10 \times log \left(\frac{6h}{\lambda}\right) = 7.7 \, dB \tag{1.8}$$

This theory relies on the notion and hypothesis that the turbulent boundary layer eddy only generates noise associated with the trailing edge-of the blade when when it forms in a direction normal to the natural edge of the blade. Since a sawtooth serration is very seldom aligned with the natural trailing-edge of the blade, it was predicted to greater reduce the noise produced when compared to a sinusoidal edge which periodically approaches and retreats from a state parallel to the span. Therefore, sawtooth serrations are more effective at reducing trailing-edge eddy noise, and are used at an angle less than 45 degrees from the streamwise flow direction [23].

$$S_{pp}^{TE}(r,\theta,\omega) = \frac{\omega c}{2ar}^{2} \Delta R D(\theta,\phi)|I|^2 \phi_{pp} I_y \tag{1.9}$$

Another mathematical model of serrated trailing-edge noise, quantifies the power spectral density of the trailing-edge noise, shown in Equation 1.9. In this equation the parameters θ, ϕ, and r describe the location of the observer relative to the center of the rotor. The variable ϕ_{pp} is the power spectral density of the wall pressure for a blade of span ΔR and chord length c [24]. This equation's dependence on pressure at the trailing-edge could account for the benefit found through the implementation of serrations on the trailing-edge of rotors as the distribution of pressure along this edge is highly dependent on the profile and size of the serrations.

1.3 Objectives & Scope

The primary objective of this study is to characterize the benefits of the addition of trailing-edge serrations on a coaxial counter-rotating rotor system. This characterization includes the aerodynamic, acoustic, and flow field evaluation experiments that were carried out to outline the differences between the baseline and the serrated trailing-edge case. Aspects of the blade geometry that were found to be beneficial to the sound emission of the rotor are to be explored further in the future in order to more effectively exploit their most useful features. Specific objectives that lead to the completion of this goal are listed below.

1. **Objective 1**: Quantify the effect of trailing-edge serrations on a coaxial rotor in hover
   (a) Quantify the aerodynamic forces and moments for both serrated and baseline rotor blades.

(b) Quantify the axial flow using PIV to compare the downwash below a serrated and baseline coaxial rotor.

2. **Objective 2**: Measure acoustic data and identify relations between acoustic measurements and flow field

   (a) Analyze overall sound pressure level and frequency spectrum created by different rotational rates for both serrated and baseline rotor blades.

   (b) Correlate the axial flow PIV measurements to the monopole, dipole, and quadrupole noise sources created by a coaxial counter-rotating rotor.

The work in this study aims to analyze improvements that can be made to current UAV rotor blades. This study utilized two experimental rotor test stands in order to evaluate the acoustic and aerodynamic characteristics of rotor blades with two trailing-edge designs. The methods used to evaluate the performance of this system included strain gauge measurements, free-field microphone measurements, and particle image velocimetry. Together, these methods were successful in evaluating the variance between serrated and baseline rotor blades.

Chapter 2

Methods

2.1 Experimental Setups

Over the course of this investigation, the setup used to gather aerodynamic, acoustic, and PIV data evolved in order to better facilitate the collection of useful data. While many changes were made over the course of this evolution, there are a few aspects of the setup that remained the same. These similarities include two counter-rotating rotor heads that can accommodate a variety of rotor blades. Both systems are driven by a single motor that mechanically links, via a gear system, the upper and lower rotors. These systems are also designed to minimize disturbances in the inflow and downwash region by reducing the planform area of structural elements used to support the rotor bearings and other mechanical elements.

2.1.1 Coaxial Rotor with Pitch Control

The first coaxial counter-rotating test stand used in this study was designed to observe the acoustic effects of the addition of serrated trailing edges to rectangular rotor blades with a fixed pitch. Both the upper and lower rotor are driven by a single Maxon flat EC60 motor that drives the inner shaft (connected to the upper rotor) which connects to a series of three gears of equal size, used to reverse the direction of the outer shaft (connected to the lower rotor). This motor was driven by a 3-phase electronic speed controller, which received voltage signals from a user-controlled potentiometer to determine the rotational rate. This rotational rate was then interpreted by built-in Hall effect sensors, and displayed on the LabVIEW software in real-time. This rotor system is supported by eight strain gauge beam load cells that were radially mounted with respect to the rotor shaft as pictured in Figure

2.1. Four of these load cells are mounted with their sensing direction oriented vertically which allows them to deflect when a thrust load is applied. The remaining four load cells are oriented laterally which allows them to deflect when a torque is applied with respect to the center rotor shaft. This load/torque measurement system allows for the acquisition of the combined torque and thrust imparted by the coaxial rotor. While this method of measuring loads was useful for acquiring combined forces and moments imparted on the system, it was not possible to record the thrust or torque values of a single rotor while operating the entire coaxial rotor.

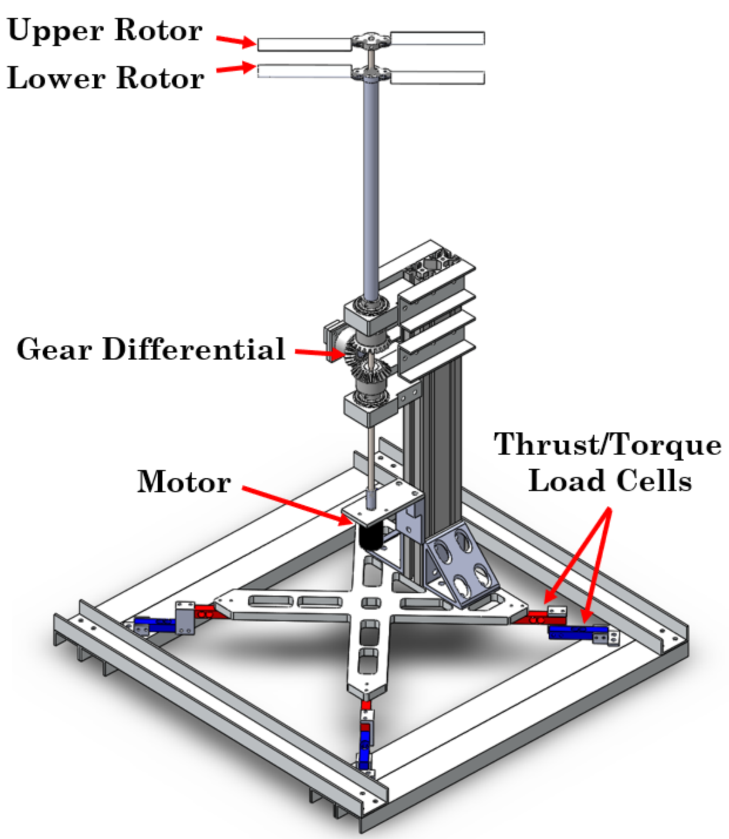

Figure 2.1: Coaxial rotor with pitch control for study of acoustics of coaxial counter-rotating rotors

Table 2.1: Coaxial Rotor with Pitch Control Specifications

R	RC	c	A_{Blades}	A_{Disc}	AR	z
175 mm	0.14r	29 mm	171.4 cm^2	962.1 cm^2	5.28	0.1 D

2.1.2 Coaxial Rotor with Twisted Blades

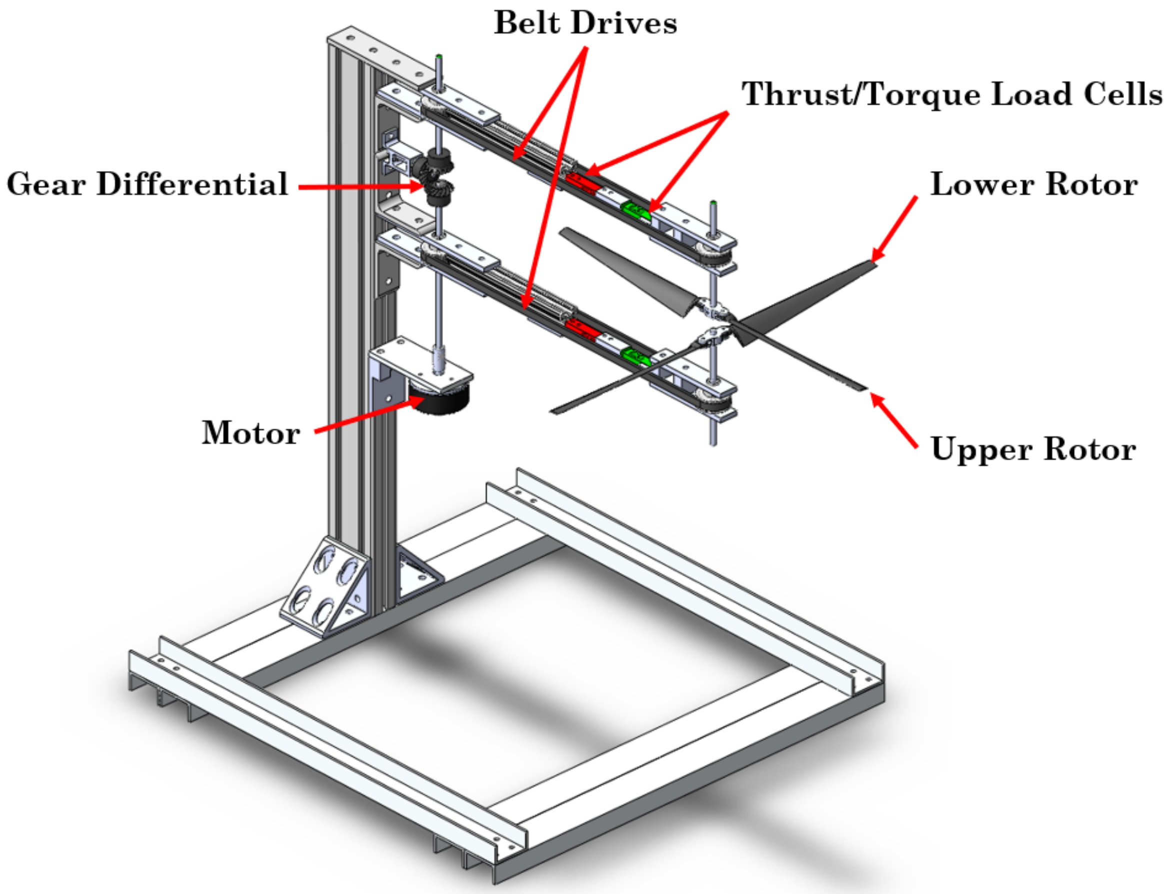

Figure 2.2: Coaxial rotor with twisted blades for independent thrust and torque measurement of upper and lower rotors

Table 2.2: Coaxial Rotor with Twisted Blades Specifications

R	RC	c (Root-Tip)	α (Root-Tip)	A_{Blades}	A_{Disc}	AR	z
250 mm	0.12r	29-14 mm	35°-8°	183.2 cm^2	1963.5 cm^2	10.56	0.1 D

The second experimental test stand, shown in Figure 2.2 used in this study was built from the same base and electronic drive system as the first test stand. Modifications made to this system address some of the flaws that were evident in final testing of the first experimental setup. The inability of the system to measure independent thrust and torque for the upper and lower rotors was the most pressing issue. This deficiency was solved by the implementation of a belt-driven system that effectively displaced the upper and lower rotor shafts from the upper and lower drive shafts by 0.45 meters. This displacement served the dual purpose of eliminating downwash disturbances on one side of the rotor as well as allowing for the support arm of the upper and lower rotor assemblies to double as a torque and thrust measurement system. The lower rotor plane was placed a distance of two diameters above the floor in order to avoid ground effect.

2.1.3 Blade Design

The main independent variable in this study was the geometry of the blades, therefore, consistency in this aspect of the experimental design was of the utmost importance. For this reason, every blade used in this study was manufactured by the additive process of 3D printing with a nylon-carbon fiber blended filament known as Onyx. The MarkForged printer used to manufacture these blades prints with a resolution thickness of $100\mu m$ layers. This resolution, along with a vertical printing technique allowed for a smooth blade profile to be achieved.

The design of these printed blades was determined through the analysis of various past studies. In some studies it was shown that the "sharper" functions used on the leading/trailing edge correlated to more effective noise attenuation. For example, a sine function would be less effective than a regular sawtooth in this respect [23]. In addition, serrations with high amplitudes and short wavelengths were identified as the most acoustically beneficial [25].

The blades used with the pitch control coaxial rotor setup were designed as a set of rectangular planform blades with the section of a NACA 0015. This set of blades consisted of positive and negative pitched blades that were used for the counter-clockwise and clockwise rotating rotors, respectively. The blades shown in Figure 2.3 are both positive pitch blades made for the counter-clockwise rotor. All rectangular blades used in this study have an equal projected blade area between the baseline and serrated blade models. This equality is essential, as in many other studies the projected area differs between the baseline and the modified blade. This difference is a result of the addition or subtraction of material and therefore total blade area in order to create serrations.

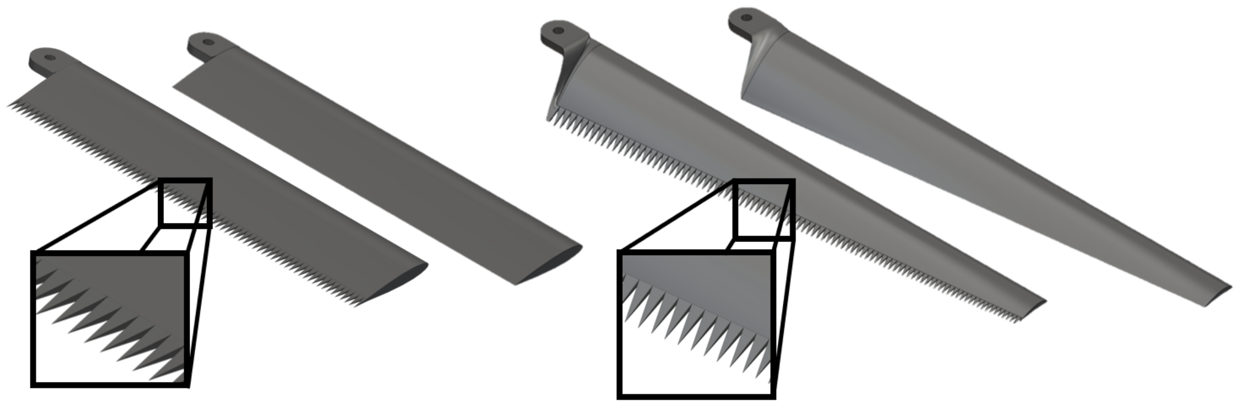

Figure 2.3: CAD models of 3D printed pitch control blades serrated and baseline (left), and twisted blades serrated and baseline (right)

Along with the mechanical modifications made in the transition from the first to the second experimental setup, significant modifications were made to the 3D printed rotor blades. Once the data from the first experimental setup, and the rectangular blades had been processed and evaluated, the need to obtain data from a more realistic model of a small-scale UAV became evident. The majority of UAVs that are currently used in industry and recreation utilize twisted blades with chord that decreases with increasing radius. In addition, most UAV rotor blades are built on an airfoil section is cambered. In the second experimental setup, rotor blades with all of the previously mentioned upgrades, were manufactured. These updated rotor blades, built from a NACA 6409 airfoil cross section, are shown in Figure 2.3.

2.1.4 Force and Moment Instrumentation

The configuration of the basic force and moment measurement system is shown in Figure 2.4. The first element in the force and moment acquisition system is the machined aluminum beam load cells. Each of the beam load cells used to translate physical strain into a dynamic voltage signal had a maximum load rating of 1 kg. Each load cell was powered externally by a 5 volt power supply. The signal from each of the load cells was filtered, amplified and filtered again by a set of four single-channel DMD4059 strain gauge signal conditioners manufactured by Omega. The output from these four signal conditioners was routed to a single National Instruments USB-6218 Data Acquisition Module, which was used to interpret and record the conditioned signals. The data acquisition software, LabVIEW, sampled the force and moment measurements at 1000 Hz and was used to view and record the data for processing.

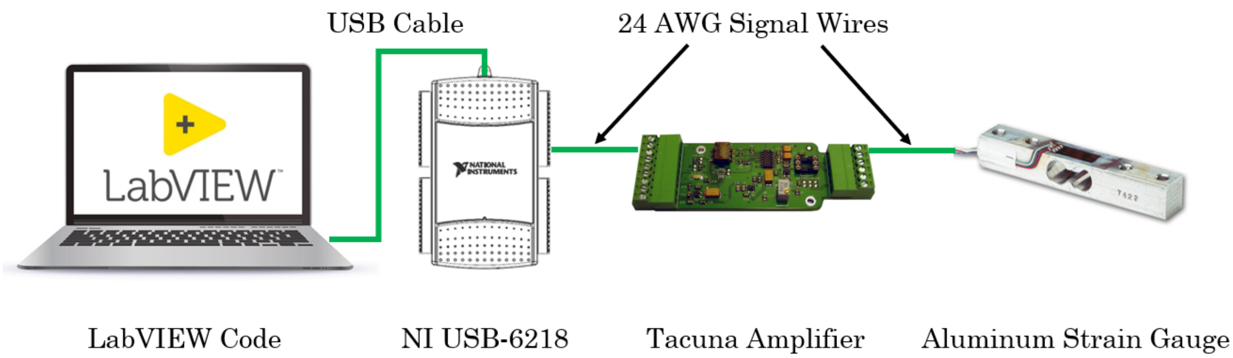

Figure 2.4: Wiring diagram of force and moment instrumentation

The calibration of the force and moment acquisition systems for both the pitch control and the twisted blade test stands were completed with the application of a weighted pulley system. This calibration was completed by loading the thrust axis while calibrating about the torque axis, and vice versa. This method allowed for the confirmation of minimal interference between signals, which was confirmed to be below 1%. The torque calibration was completed through the use of a moment arm and a weighted pulley. This system simulates a moment at 6 inches from the rotational axis and an upward thrust centered about the axis of rotation. The plots from these calibrations are shown in Figure 2.5. Non-linearity in the thrust calibration was identified, and attributed to the magnitude of the static load incident on the moment arm.

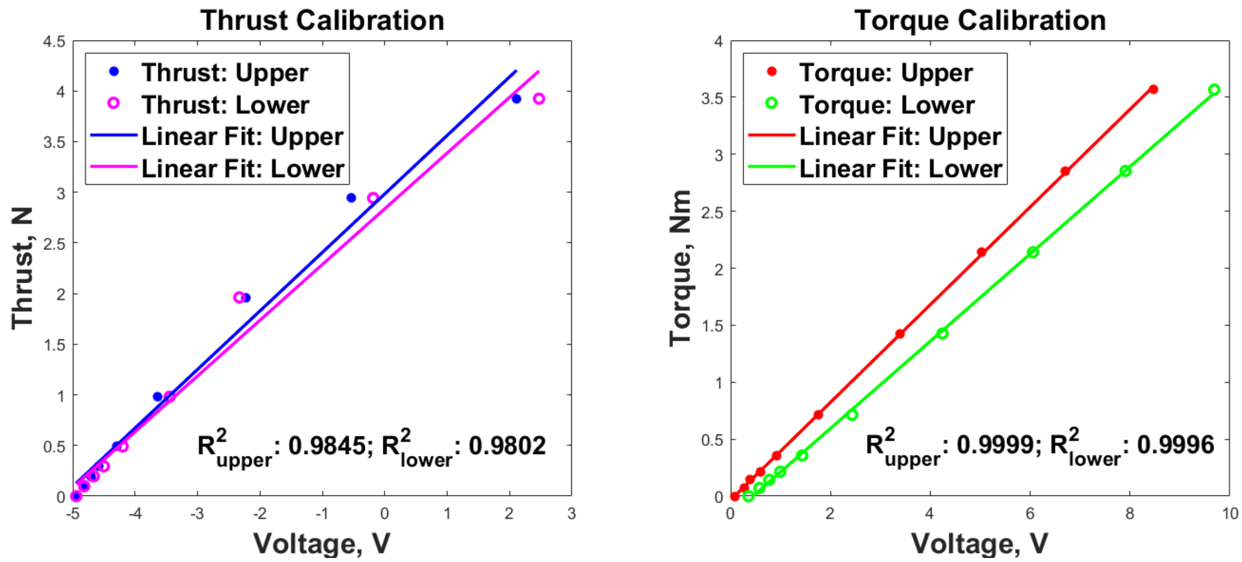

Figure 2.5: Calibration plots for thrust and torque

2.1.5 Acoustic Instrumentation

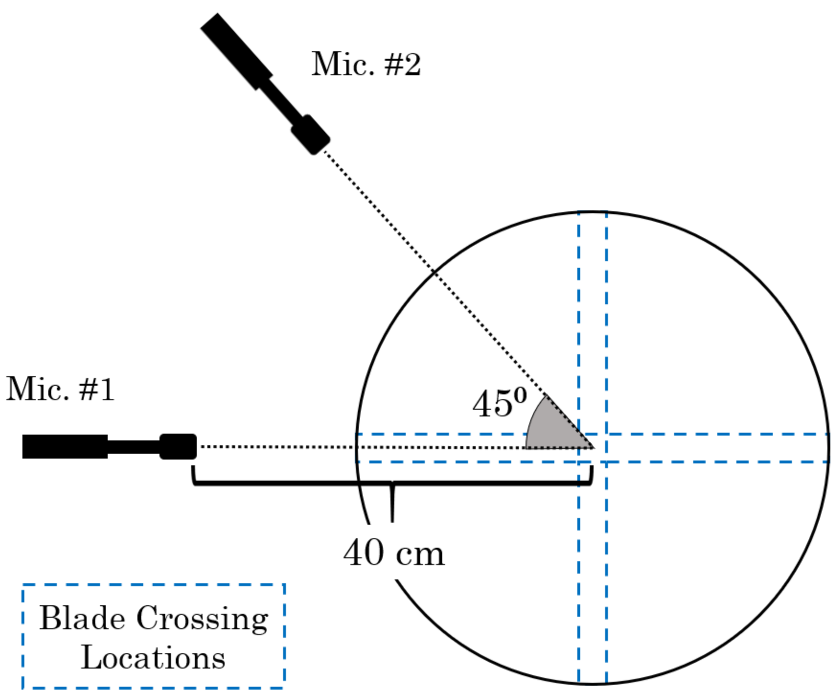

Figure 2.6: Aerial view of rotor plane and microphone arrangement of the pitch control coaxial rotor setup

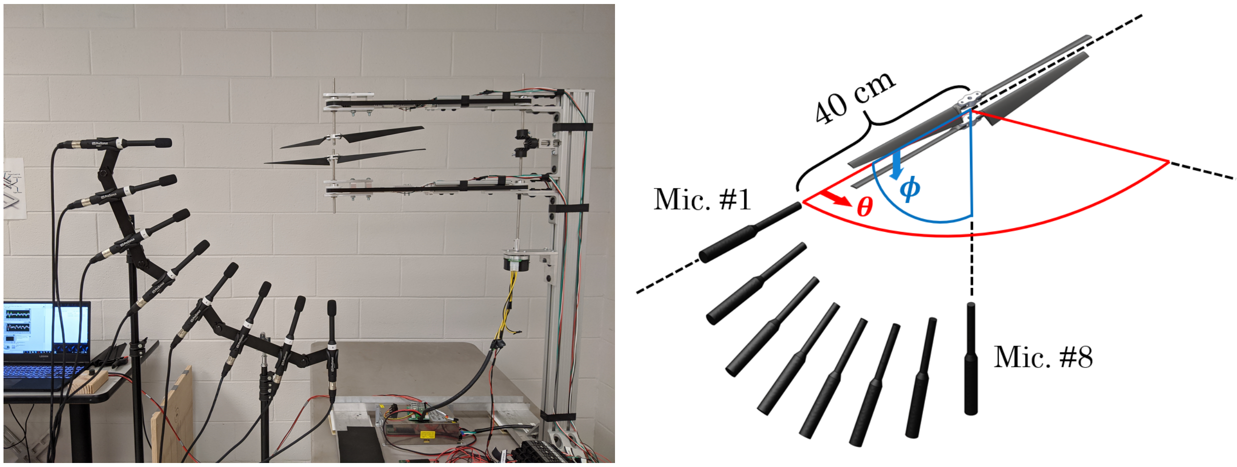

(a) (b)

Figure 2.7: (a) Microphone array configuration used for acoustic data acquisition of the second experimental setup; (b) Microphone array configuration graphic for angles θ and ϕ

The acoustic data that was collected from the pitch control coaxial rotor was acquired from an array of two free-field measurement microphones shown in Figure 2.6. The placement of these microphones was chosen to determine how the addition of serrations as well as proximity to the blade crossing location affects the acoustic signature. Both microphones were affixed halfway in-between the upper and lower rotor planes in order to avoid excess turbulence noise caused by high velocity downwash or outwash air flows passing by the microphone heads.

The improved microphone array, shown in Figure 2.7, used in tandem with the coaxial rotor with twisted blades setup is supported by two microphone stands that each hold four microphones. Together, these eight microphones form an arc that spans the 90 degrees of latitude angles below the rotor plane. This array was specifically designed to capture the sounds created by multiple acoustic noise sources. By design, the microphones directly below the rotor plane captured the highest proportion of loading noise, while the microphones that align closely with the rotor plane captured most of the thickness noise. All intermediate microphones were placed to capture other extraneous noise sources such as blade vortex interaction noise.

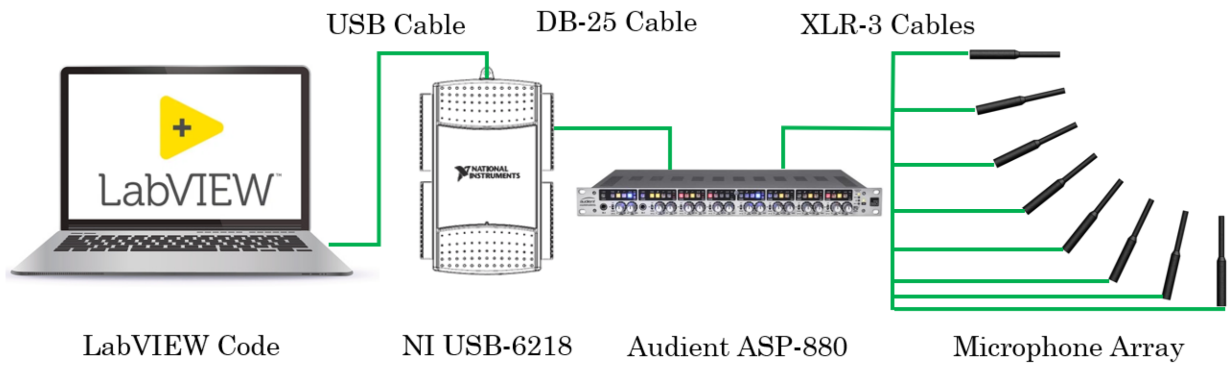

Figure 2.8: Wiring diagram of acoustic instrumentation

The eight microphones used in this study are all 1/2-inch free-field measurement microphones manufactured by PreSonus. These microphones have a sensitivity of 14 mV/Pa, a peak sound pressure level of 132 dB, and a frequency range from 20 to 20,000 Hz. Each microphone was linked with XLR 3 cable, as shown in Figure 2.8, to the Audient ASP-880 pre-amplifier system. This system amplified the audio signal by a user-adjustable factor. The gain setting for all experiments was set to 48 dB. This setting allowed the microphones to maintain a large dynamic range that encompassed the active decibel range. The high-pass filtering available on the amplification system was not utilized. The amplified audio signal that exits the pre-amplifier system was then sent to the USB-6218 Data Acquisition Module where the data was routed to LabVIEW.

Moving to the calibration of the microphones, each microphone was calibrated individually before being combined into an array. Calibration was completed with a Reed R8090 two-level sound calibrator, which provides two data points for calibration, one at 94 dB and the other at 114 dB. This two-point calibration, shown in Figure 2.9, was sufficient for a microphone as the variation of output voltage with SPL will always be logarithmic. Therefore, when the calibration results are plotted on a logarithmic axis, the result will be linear. The microphones used in this experiment come pre-calibrated by the manufacturer, however the acquisition system for this experiment differs from traditional acoustic equipment. Therefore, additional calibration was necessary in order to ensure that accurate measurements

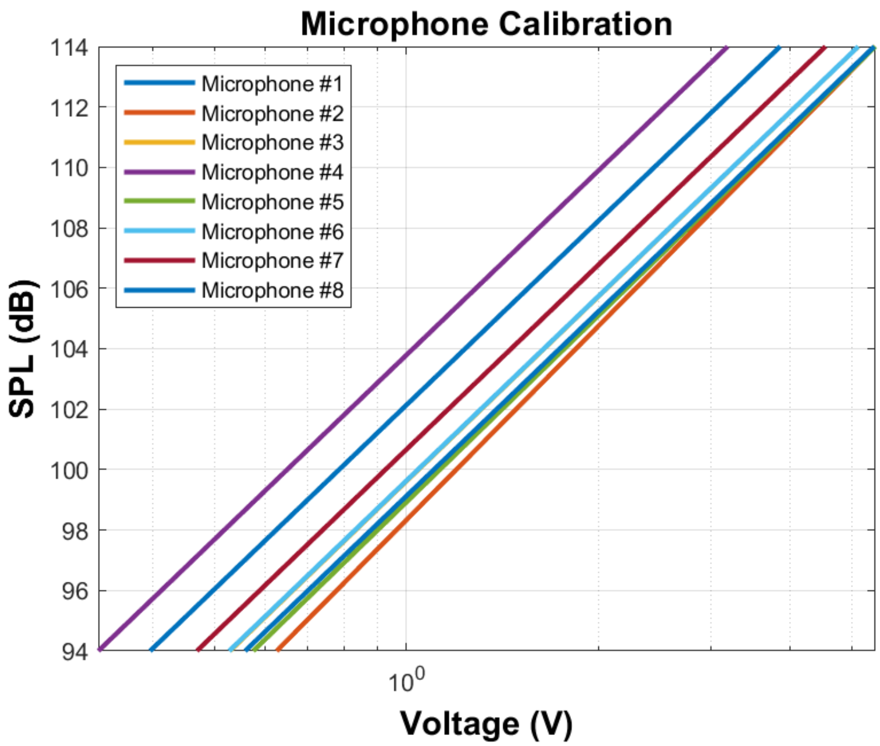

Figure 2.9: Logarithmic plots of each microphone calibration curve, displaying variation of voltage with simulated SPL

were being made. While variations in voltage offset between individual microphones were identified, they were confirmed to be consistent between multiple calibration trials, resulting in a maximum uncertainty in measured SPL of 0.06 dB.

2.1.6 PIV Instrumentation and Processing

The flow field was evaluated using a planar PIV with two 4MP Vision Research VEO 640S (1400 fps) cameras with a resolution of 2560×1600 pixels. The wiring diagram of this setup is shown in Figure 2.10. These cameras each viewed an area measuring approximately 0.24 m $\times$ 0.18 m (0.48 D $\times$ 0.36 D). A Photonics dual head laser (527 nm wavelength with pulse energy of 30 mJ/pulse at 1 kHz) operating in peer mode was used to produce the laser sheet through the use of the combination of a collimator and cylindrical lenses. A total of 2000 images were acquired for each test case at the rate of 700Hz. The time difference (δt) between the pulses were optimized for each case, by maintaining a constant proportion between rotational frequency and time difference across the three rotational rates. The δt used for rotational rates 750, 1000, and 1250 RPM were 333, 250, and 200μs respectively. A custom-designed and CNC machined aluminum calibration plate was used for the calibration of the field of view. The lenses used in this study were both Nikon 50 millimeter fixed-focal length lenses set to an f-number of f/1.8. The seeding particles used were comprised of a water and glycerin-based fluid that was heated using a traditional fog machine.

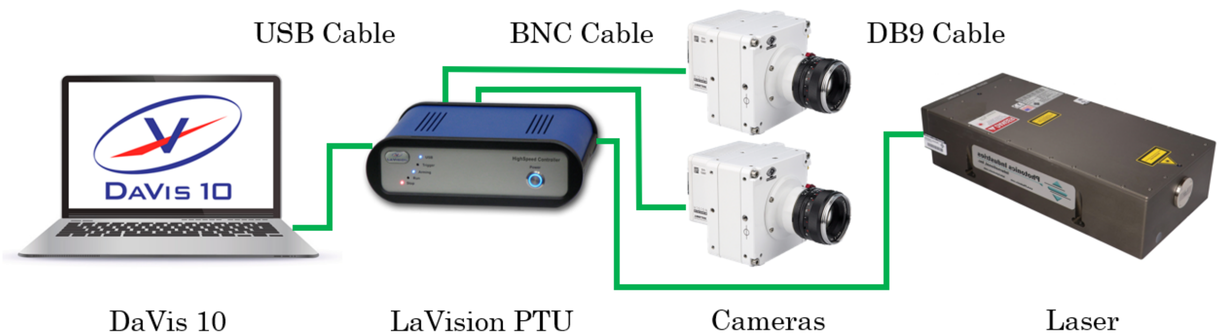

Figure 2.10: Diagram of PIV instrumentation wiring

PIV data was acquired and processed using DaVis 10 imaging software. This software used the images recorded from double frame PIV acquisition to cross correlate the location of individual particles from the first double frame image to the next. This cross correlation was carried out for an interrogation window of size 128×128 pixels with the second pass using a window size of 64×64 pixels. Each pass used an overlap ratio of 75%. The velocities that were obtained for each pixel area were then averaged with respect to time to create a time-averaged flow field. Later, velocity profile plots were created by taking a horizontal slice of the y-component of the velocity field data and plotting against the radial location.

2.1.7 PIV Uncertainty

The error from this system was quantified using the built-in DaVis calibration method. This error quantification method used a 2-dimensional calibration plate that was placed in the same plane as the laser sheet. Image processing included background noise reduction by subtracting the sliding average from the raw image. The velocity fields were then obtained by processing the images using the multi-grid, multi-pass cross-correlation technique. Vector fields were post-processed to remove spurious vectors which were then stitched together to obtain the final flow field. The uncertainties in the velocity measurements were quantified using the correlation statistics method [27], where the uncertainty is proportional to the residual positional disparity between the matched correlation peaks [28]. The dt in this study was selected such that the out-of-plane motion of particles was minimized. The resulting uncertainty in the velocity across the flow field for all cases were observed to be less than 1% of the average velocity in the flow field.

2.1.8 PIV Configuration

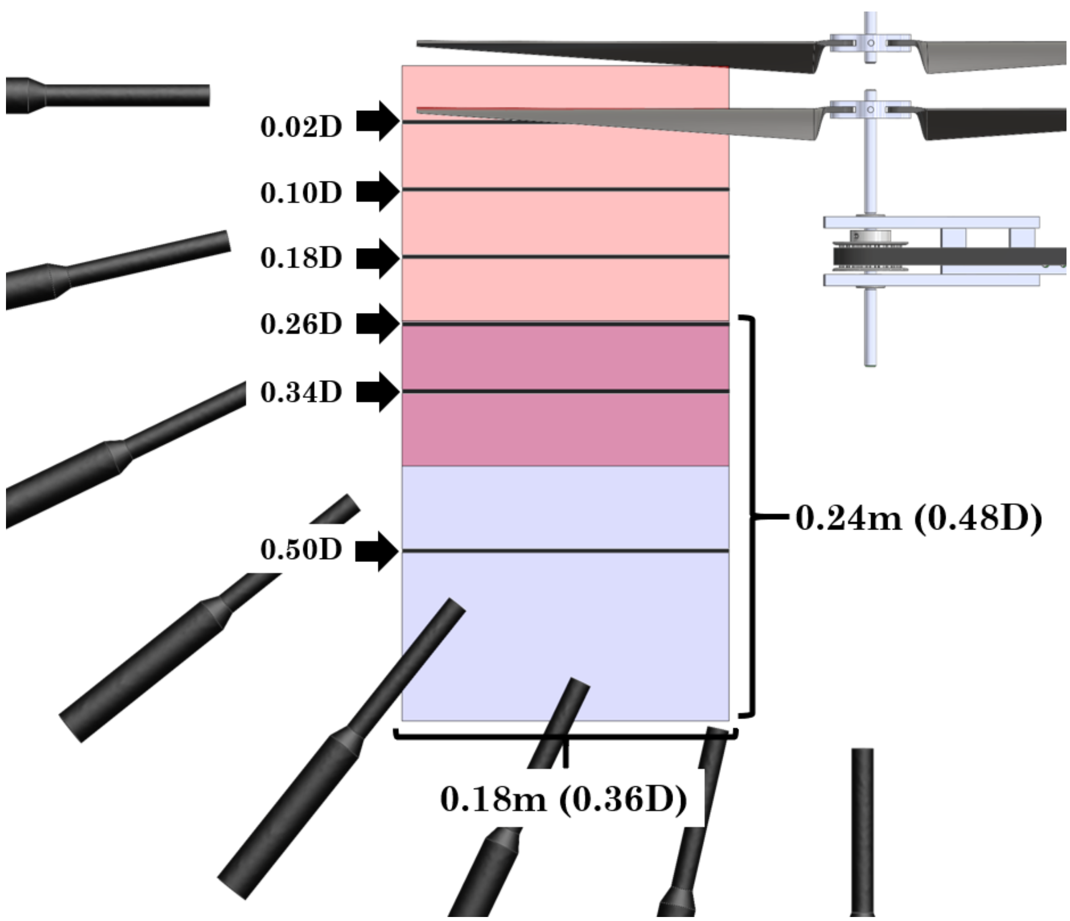

Figure 2.11: Upper and lower PIV frames shown in red and blue, respectively. Six levels below lower rotor plane used to analyze velocity profiles

One set of flow field analysis tests were conducted on the second experimental setup, which used the method of PIV. This test served to clarify the physical flow mechanisms by which acoustic differences were caused. Specifically, the velocity below the rotor as well as the turbulence induced by the rotors were studied.

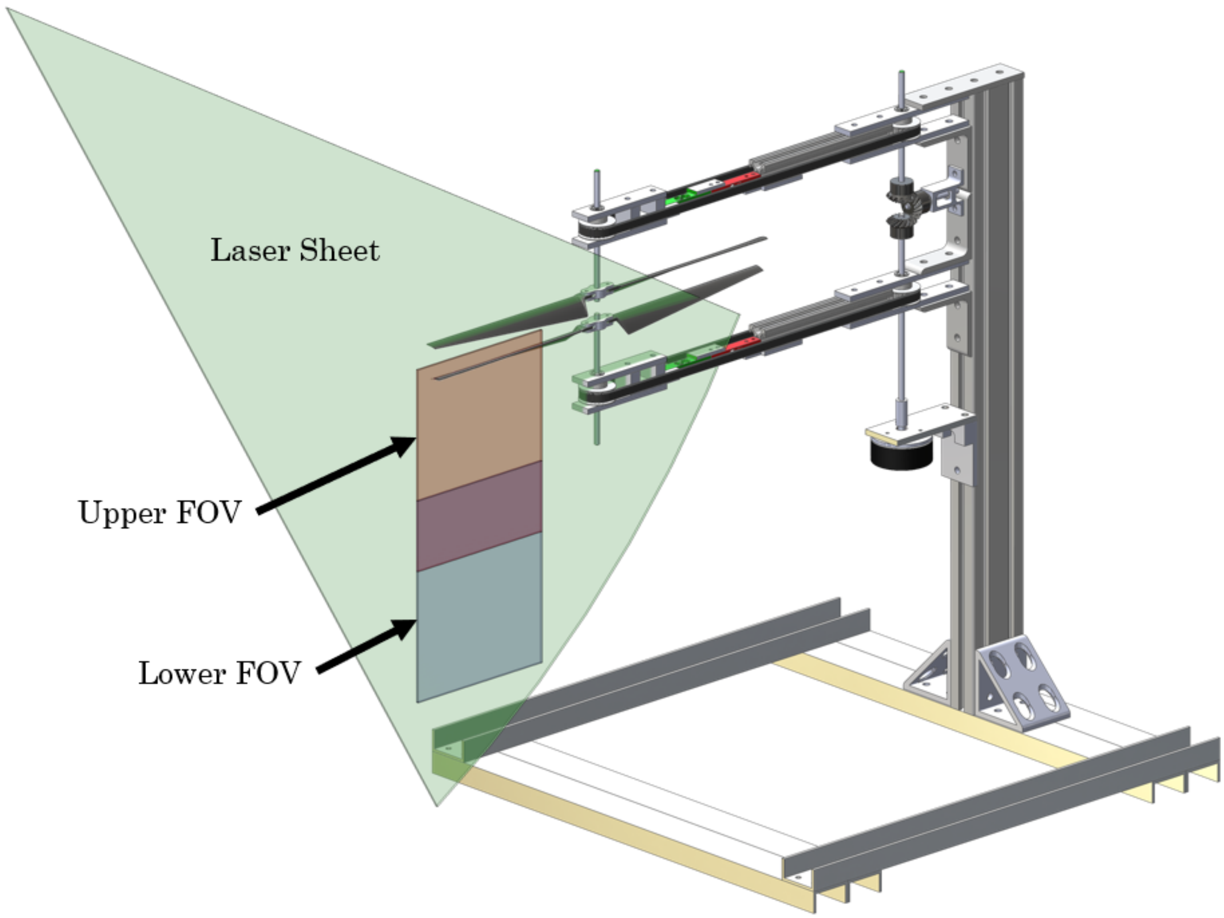

Figure 2.12: Axial velocity PIV configuration to assess downwash velocity and microphone interaction; displaying laser sheet, and upper and lower PIV fields of view in red and blue, respectively

The PIV configuration used was referred to as the axial velocity configuration, and is shown in Figure 2.12. This configuration consists of a laser sheet that shines directly on the center axis of rotation of both the upper and lower rotor shafts. The angle at which the laser was positioned allowed for full coverage of each field of view.

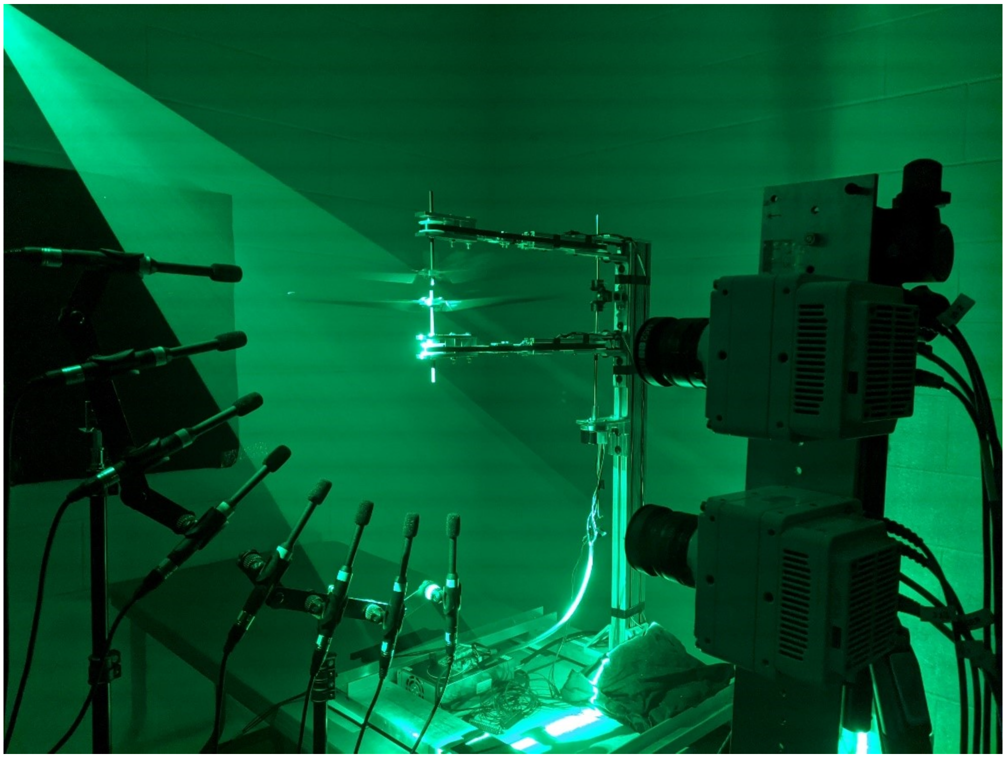

Figure 2.13: Axial velocity PIV setup photograph

The upper and lower cameras were placed in a vertical arrangement, as shown in Figure 2.13, to capture two different areas of interest. The upper camera captured both the formation of tip vortices and the velocity profiles that formed the downwash. The lower frame further tracked these velocity profiles as well as the evolution of turbulence intensity below the rotor. The lower frame also encompassed the tips of microphones 5 and 6 as reference points. However, in this specific experiment, the microphone array was shifted 2cm away from the plane in which PIV was conducted, in order to mark the position of the microphones while avoiding extra flow disturbances.

2.2 Data Analysis

Post-processing of aerodynamic and acoustic data were accomplished through the use of MATLAB. Aerodynamic force and moment data acquired and recorded by LabVIEW was transferred into excel spreadsheets. These spreadsheets were read by MATLAB where the average values for torque and thrust of each set of test conditions were calculated. These values were then plotted using MATLAB. The error from this system was quantified using calibrations weights and a moment-arm calibration system.

Acoustic data was also processed using MATLAB. In order to find OASPL values, the high-frequency voltage signal from the microphone amplifier was saved as an excel sheet for each set of experimental conditions. This excel sheet was read using MATLAB, where the average amplitude was calculated and then substituted into a logarithmic calibration function for each microphone.

Frequency spectrum data were acquired through the use of the "fft" function in MATLAB as well as the previously mentioned calibration points. Each frequency spectrum shown was averaged using an incrementally-shifted averaging technique. In this method, each 400,000 sample dataset was broken into sets of 40,000 samples. Each of these sets of samples overlapped the last set by 39,900 samples. The Fourier transform of each set was determined, and subsequently averaged together for each test condition.

MHSPL values were solved for in a similar fashion, by isolating the frequencies from 4,000 to 12,800 Hz and subsequently using the method shown in Equation 1.3 which derives its method from the classical equation for sound pressure level from Equation 1.1.

The error from the acoustic readings was quantified through the comparison of the linear regression of the microphone calibration and the theoretical sound pressure level curve. Comparing subsequent trials of microphone calibrations, the error between trials was found to be less than 0.06 dB.

$$R_A(f) = \frac{12200^2 f^4}{(f^2 + 20.6^2)\sqrt{(f^2 + 107.7^2)(f^2 + 737.9^2)}(f^2 + 12200^2)} \tag{2.1}$$

$$A = 2.0 + 20log(R_A(f)) \tag{2.2}$$

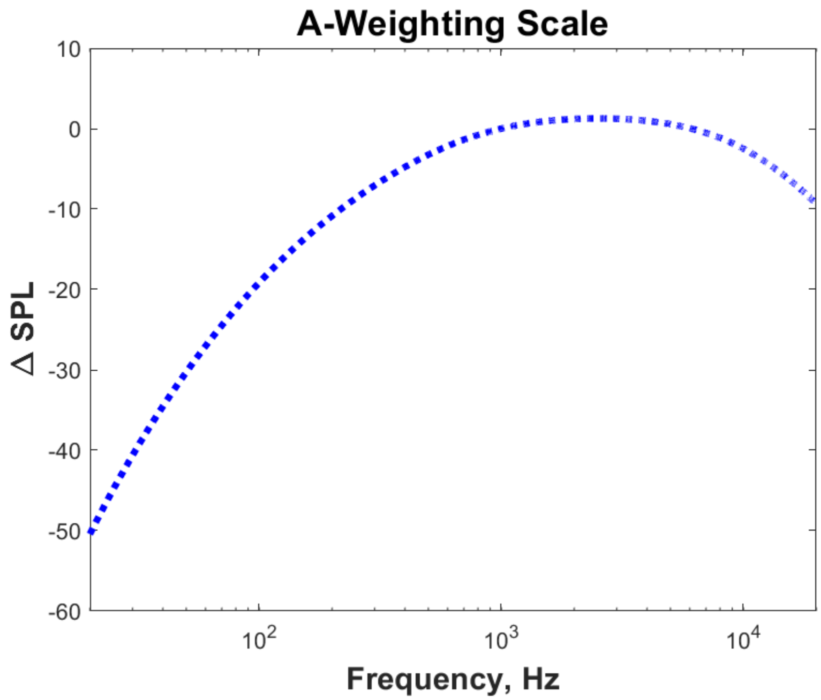

Figure 2.14: A-weighting scale of sound pressure level with respect to the human hearing spectrum

A useful and necessary step in the analysis of acoustic signals in the presence of human ears is an understanding of A-weighting. The A-weighting function was developed as a method to estimate how humans interpret acoustic intensity across the audible frequency spectrum from 20 to 20,000 Hz. The two equations used in this analysis are shown in Equations 2.1 and 2.2 [26]. This function plotted against frequency is shown in Figure 2.14. While A-weighting is a useful tool for examining the effect of pressure waves on human ears, the data shown in the body of this study was left in an unweighted form. However, all A-weighted data can be found in the Appendix.

Transitioning to the PIV data, once the flow fields from multiple cases were analyzed at face value, they were further processed to quantify discrepancies between the two cases in question. The next technique utilized was the extraction of velocity profiles from the velocity fields. The velocity profiles along 6 different radial horizontal lines were pulled from the time-averaged velocity field to further verify the gradient in the two cases. This data was extracted from DaVis in the form of .dat files. These velocity values were then plotted with MATLAB.

$$u_{rms} = \sqrt{\frac{1}{N}\sum_{i=1}^{N}(u_i')^2} \tag{2.3}$$

$$TI = \frac{u_{rms}}{\bar{u}} \tag{2.4}$$

The turbulence intensity in the downwash was also evaluated using post-processed data from the velocity fields. Equation 2.3 shows the first step of calculating the turbulence intensity, which is the root mean square velocity. Equation 2.4 takes this root mean square velocity and divides it by the mean velocity along the chosen set of data. This set of operations results in turbulence intensity.

Chapter 3

Results and Discussion

3.1 Aerodynamic Results

The acquisition of aerodynamic data was the first step in the characterization of the two chosen rotor types. Both the rectangular and twisted rotor blade configurations torque and thrust values were recorded for multiple rotational speeds that were chosen due to their range of tip Reynolds numbers.

3.1.1 Aerodynamic Results for Coaxial Rotor with Pitch Control

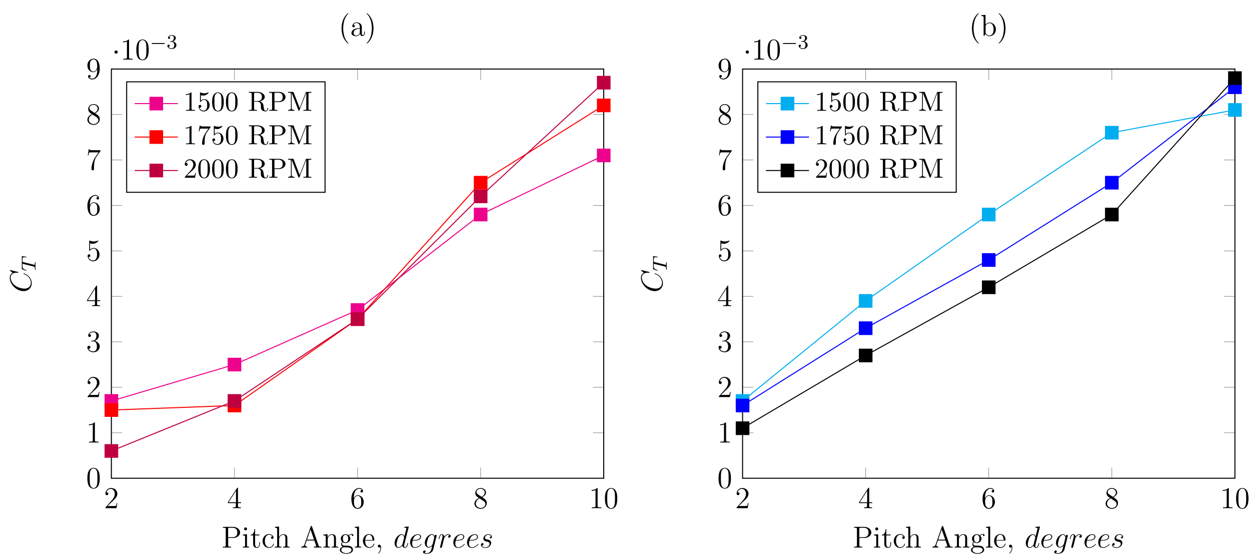

Figure 3.1: Coefficient of thrust varying with pitch angle for rotational rates form 1500 to 2000 RPM for the (a) baseline and (b) serrated cases

The goal of the aerodynamic testing was to prove that in spite of the physical changes made to the rotor blades and the aeroacoustic benefits shown, the aerodynamic performance was unaffected. The aerodynamic performance of the pitch control test stand was quantified

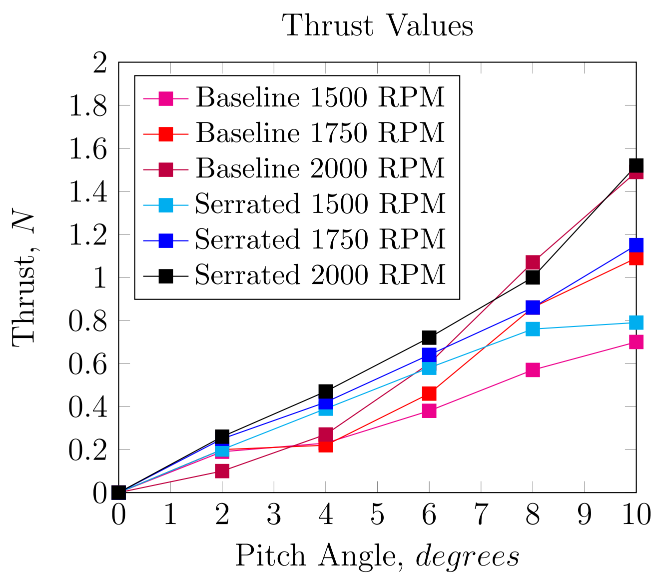

Figure 3.2: Thrust compared with pitch angle at rotational rates from 1500 to 2000 RPM for a rectangular blade for the baseline and serrated cases

using thrust coefficient C_T, which is evaluated using Equation 3.1. In this equation, T is the thrust produced in Newtons, n is the number of rotor blades, ρ is the density of air, A is the blade area, Ω is the rotational rate, and R is the radius of the rotor. While minor changes in thrust and torque values were found for a certain rotational rates, the coefficient of thrust for the test cases undergoing acoustic testing varied by only 2%. This chosen test case was set as the largest pitch angle (10°) and rotational rate (2000 RPM) tested.

$$C_T = \frac{T}{n\rho A(\Omega R)^2} \tag{3.1}$$

When thrust values were compared with pitch angle between the serrated and baseline cases a similar juxtaposition to that of C_T was made. These similarities exist due to C_T being used as a dimensionless measure of thrust produced. While the trend leading up to maximum pitch angle, and consequently, thrust production differs between the baseline and serrated cases, the cases begin to match as pitch angle and rotational rate were increased. Due to this correlation, the rotational rate of 2000 RPM and pitch angle of 10 degrees were chosen for the majority of the acoustic comparisons.

3.1.2 Aerodynamic Results for Coaxial Rotor with Twisted Blades

A similar set of aerodynamic tests were run on the twisted blade rotor test stand. However, this setup had the advantage of separate upper and lower rotor measurements. This ability provided the opportunity to observe the interactions between the upper and lower rotor. Another improvement in the collection of data for the coaxial rotor with twisted blades was the addition of averaged data sets. Each data point shown is the average of 5 trial runs (N=5) with the motor being powered down for each consecutive set. The foremost finding in the aerodynamic results show that for the separate upper and lower rotors the difference in rotor thrust between the upper and lower rotors is consistent. This difference was determined to be approximately 5% for a rotor spacing of 0.1D which was outlined in the past by [29] [30]. The proportion of the difference in this study between the rotors was between 3 and 13%. This discrepancy is most likely due to vast differences in the twist and chord length of the blades used between the two studies. The main difference between the current experimental test stand and the literature study was the twist distribution. In the comparative study, the twist varies from a maximum of 30 degrees while the current study uses a maximum of 35 degrees twist angle to match that of common UAV rotors. The span of the blade in the comparative study was also considerably longer at 0.66 m compared to the current study at 0.25 m.

The first set of plots shown in Figure 3.3 displays the thrust and torque measurements of the upper rotor taken for 6 rotational rates. These plots show the averages from three separate test trials at each rotational rate that are the averages of these three test trials. The second set of plots shown in Figure 3.4 show the corresponding thrust and torque data for the lower rotor. When comparing these two sets of plots, the main variations appear to be an offset in the torque measurements. All thrust readings between 750 and 1250 match within 4%. Due to this matching data, the rotational rates of 750, 1000, and 1250 RPM were later chosen to examine acoustic differences between the two cases.

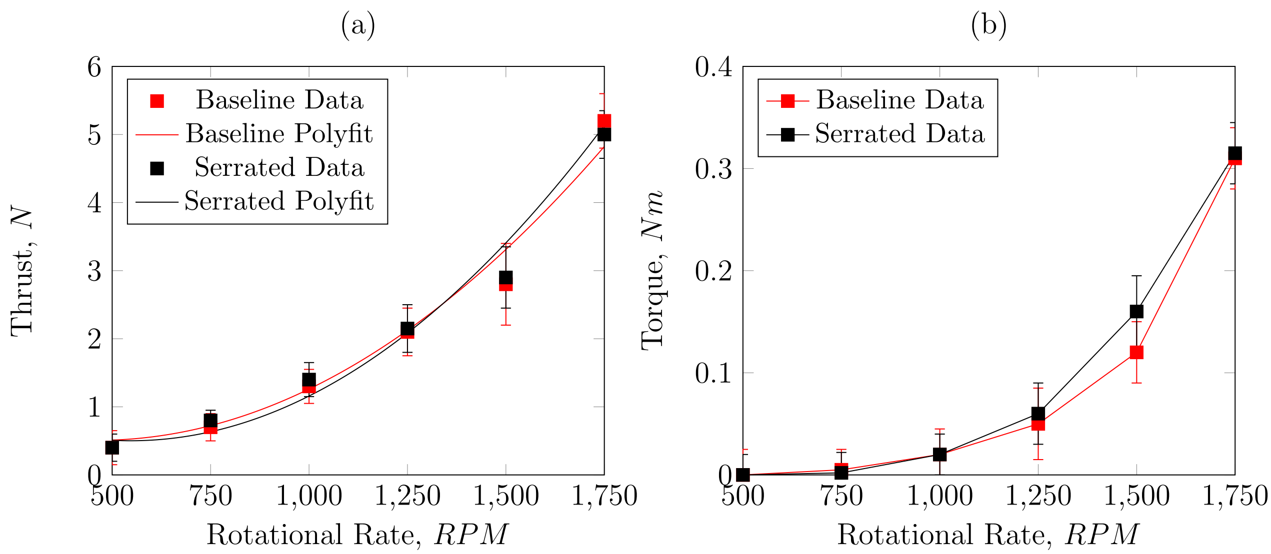

Figure 3.3: Averaged (a) Upper Rotor Thrust (with quadratic fits) and (b) Upper Rotor Torque for rotational rates between 500 and 1750 RPM of both the baseline and serrated cases with error bars denoting standard deviation of 5 trial runs

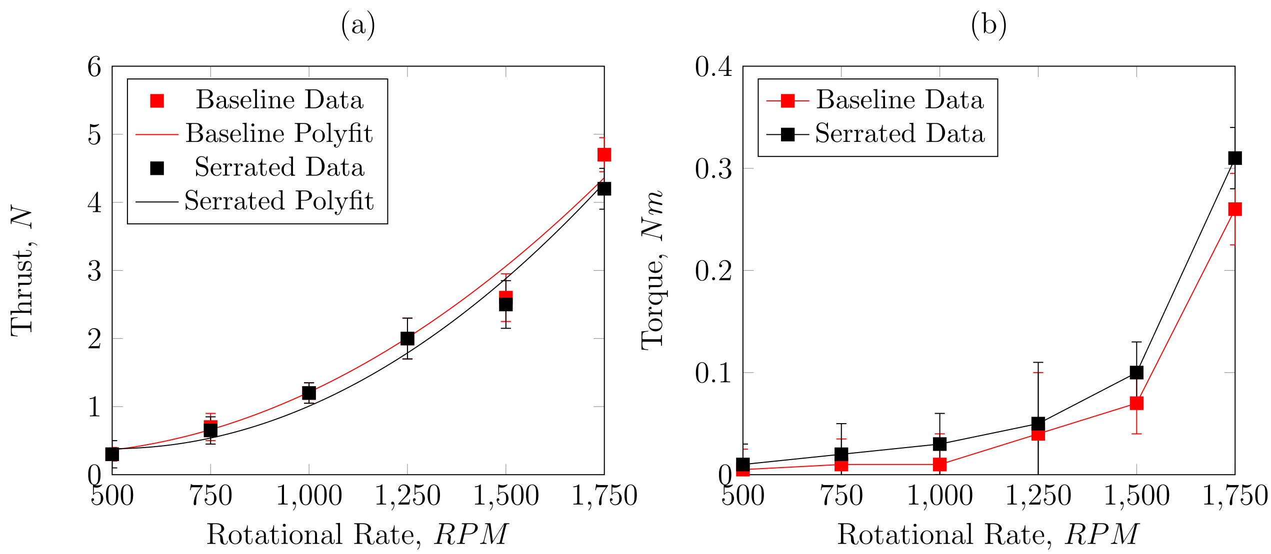

Figure 3.4: Averaged (a) Lower Rotor Thrust (with quadratic fits) and (b) Lower Rotor Torque for rotational rates between 500 and 1750 RPM of both the baseline and serrated cases with error bars denoting standard deviation of 5 trial runs

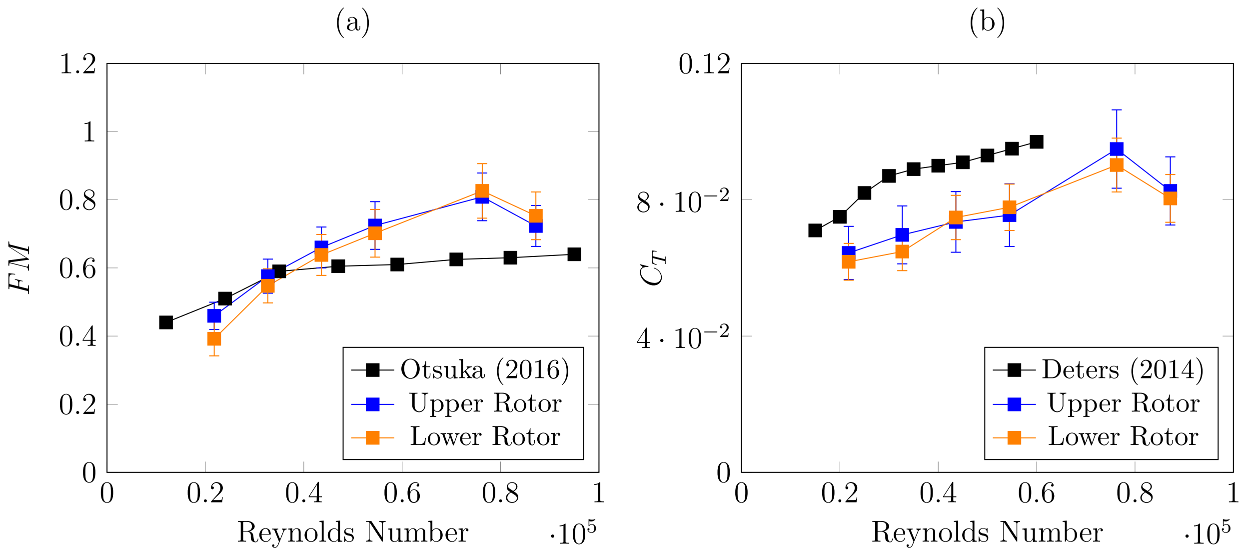

Figure 3.5: Comparison with previous studies (a) Figure of Merit with Otsuka (2016) and (b) Coefficient of Thrust with Deters (2014); Error bars denote the standard deviation of (N=5) trial runs

In Figure 3.5 two comparisons are made to prior works in the field of small-scale UAV aerodynamics. The first comparison in Figure 3.5a was made with the data from a study on twisted blades at low Reynolds number. This comparison was made by evaluating the rotor figure of merit at different rotational rates. The figure of merit (FM) was quantified using Equation 3.2. These blades were based on a NACA 6409 airfoil cross section [31]. The comparison shows that the relationship between figure of merit and Reynolds numbers varies within a certain margin, but overall, displays the same trend.

$$FM = \frac{C_T^{3/2}/\sqrt{2}}{C_Q} \tag{3.2}$$

In Figure 3.5b another comparison was made with a dataset collected in a static wind tunnel for a 2.5×0.8 propeller. These low Reynolds number conditions were also used to emulate the conditions of a small UAV, however, this particular study was geared towards forward flight [32]. While the data between the previous and current studies do not match exactly, they also show similar rates of increase in coefficient of thrust.

3.2 Acoustic Results

The first step in quantifying the acoustic performance of the rotor blades being studied was to analyze the unavoidable background noise that was present during testing. The testing facility was a non-anechoic room constructed with cinder-block walls.

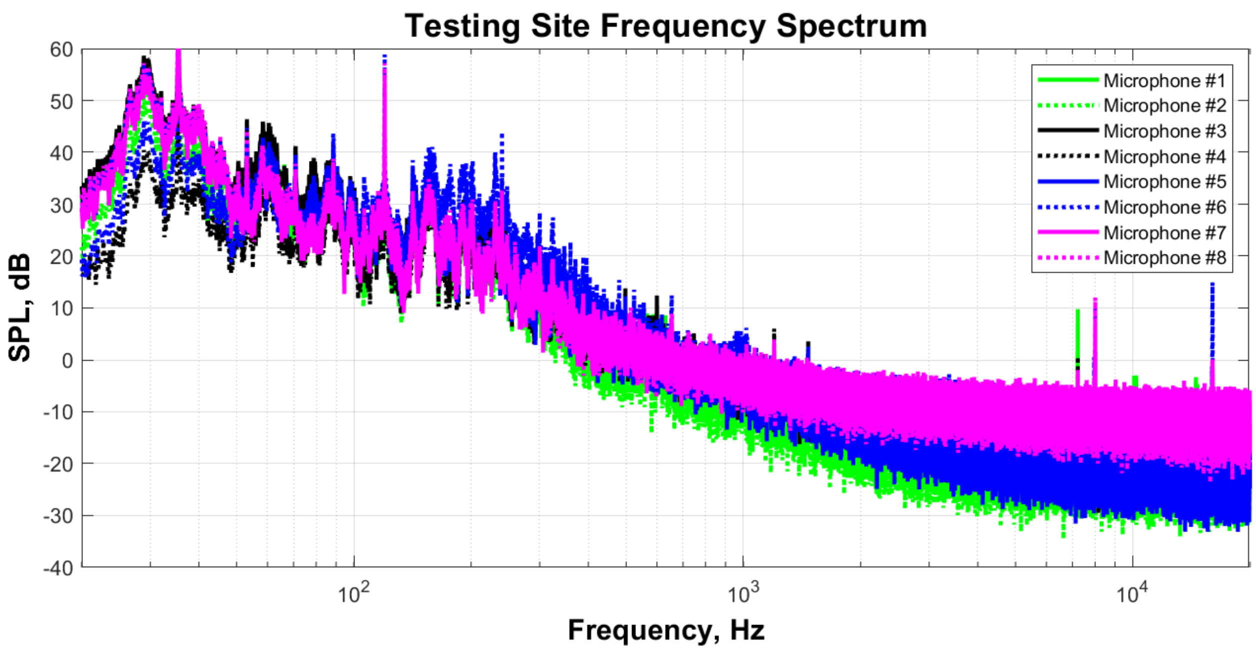

Figure 3.6: Quiet room Fourier transform frequency spectrum

The frequency spectrum of the acoustic signal captured at the testing site is shown in Figure 3.6. This measurement served to discern between sound produced by the rotor setup and sound produced by extraneous sources. Stray frequency peaks present in the testing room were attributed to the air conditioning system, noise from neighboring lab rooms, and electronic interference induced in the lengths of XLR-3 cable and signal wires used for each of the eight microphones.

3.2.1 Acoustic Results for Coaxial Rotor with Pitch Control

The majority of acoustic results shown for the rectangular blades were taken at a rotational rate of 2000 RPM, with other rotational rates shown to emphasize the effectiveness of trailing-edge serrations at this rate. Pitch angle varied between test runs in order to quantify how increased lift affects the reduction in sound produced by the blades. The range of pitch angles from two to ten degrees was chosen to simulate how the noise reduction varies through the majority of its useful range of pitch angles that precede stall at approximately 12 degrees.

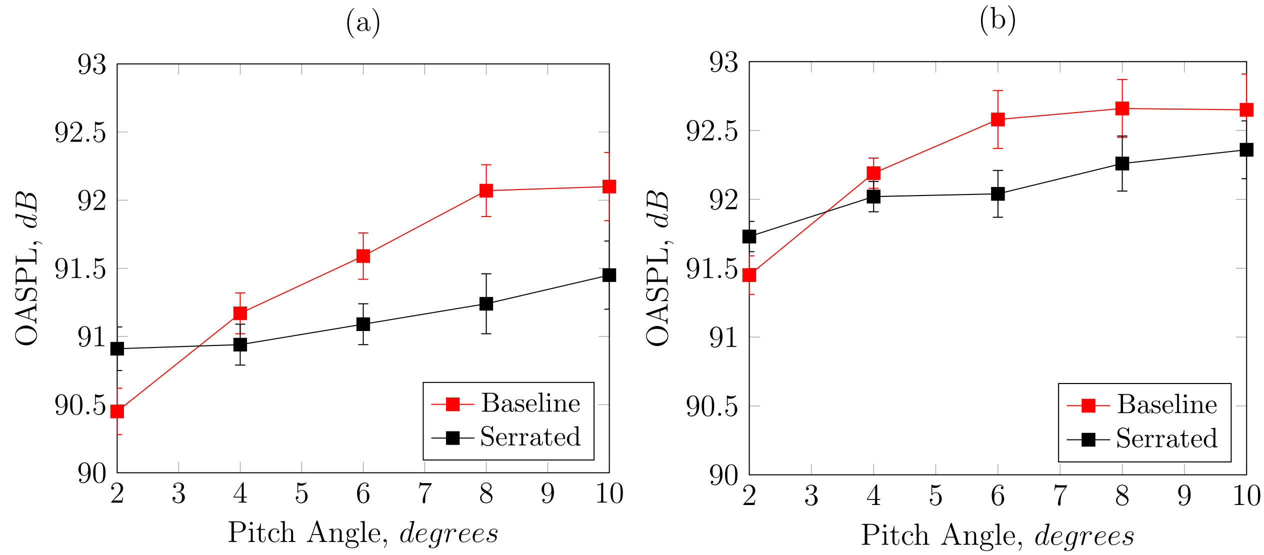

Figure 3.7: OASPL vs. pitch angles ranging from 2 to 10 degrees for (a) Microphone 1 and (b) Microphone 2 in the baseline and serrated cases. The error bars denote the standard deviation calculated between the (N=5) trial runs

The acoustic results obtained from this first experimental setup in Figure 3.7 display that as pitch angle increases, within a specified range, the benefit of trailing-edge serrations increases. The two plots shown in this figure represent the first and second microphones used in this set of data acquisition. The two microphones were placed in the configuration shown in Figure 2.6. This microphone configuration was chosen to capture two different locations relative to the location at which the upper and lower blades coincide in one vertical plane. This location is referred to as the blade crossing location. The blade crossing location typically induces an area of high pressure in between the upper and lower rotor planes. This high pressure impulse was originally hypothesized to be the cause of a higher OASPL.

However, the results gathered proved that microphone two produced a higher OASPL than microphone one regardless of pitch angle.

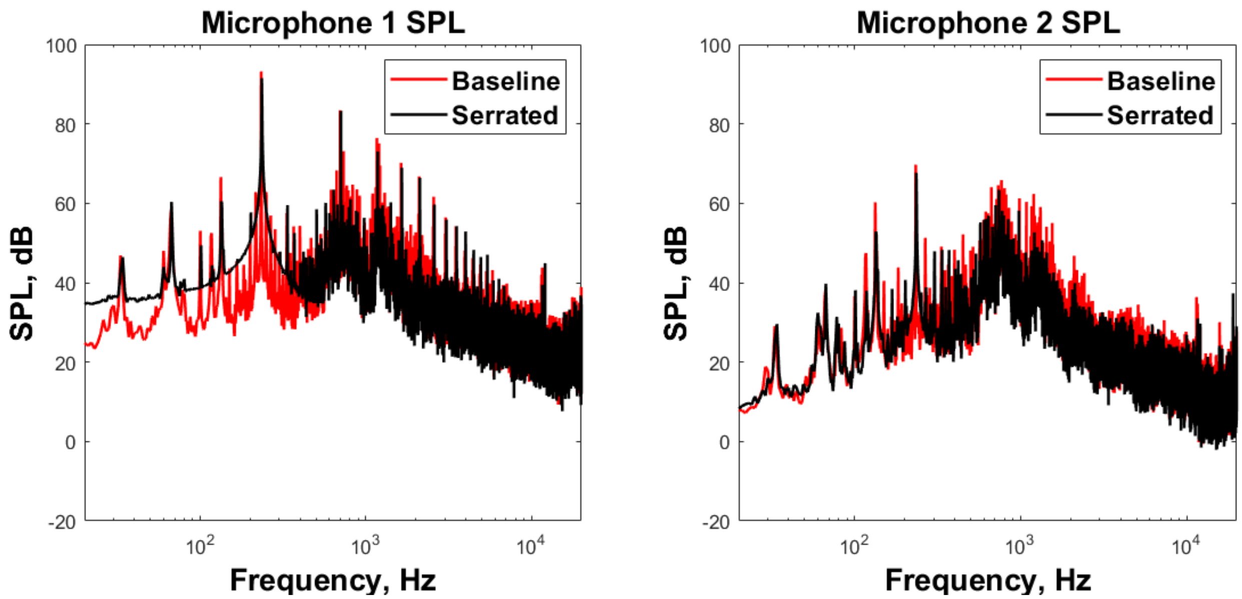

Figure 3.8: Audible frequency spectrum of pitch control rotor setup at 2000 RPM and 10 degrees pitch angle for the baseline and serrated cases

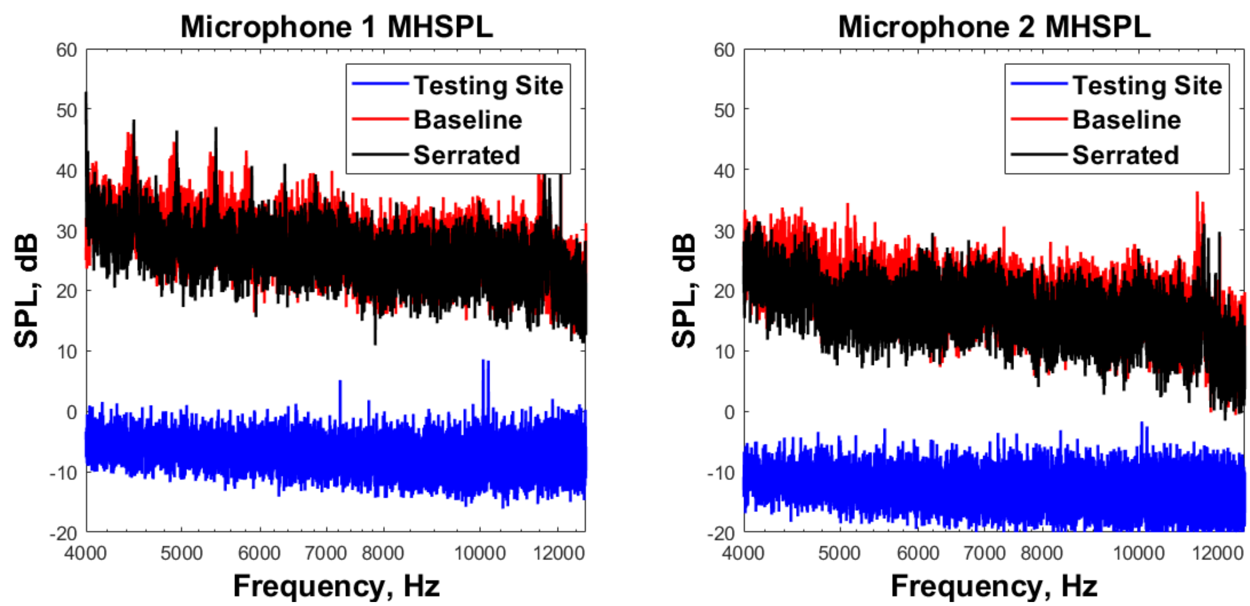

Figure 3.9: Comparison of middle-to-high frequency ranges for 10 degree pitch angle baseline and serrated blades at 2000 RPM

The next step after assessing the OASPL results was to use a Fourier transform to analyze the frequency spectra involved. Figure 3.8 shows the full audible range of frequencies for the OASPL results shown previously. In this figure, the highest peak shown is near the region associated with blade crossing frequency. A reduction in the aplitude of this blade crossing frequency is visible in both plots. After the full frequency spectrum was analyzed, another range of frequency was inspected. This range of sound pressure levels known as the MHSPL has been shown to benefit from the implementation of trailing-edge sawtooth serrations on a single rotor. However, this benefit in the middle-to-high range of frequencies was only present for the higher rotational rates tested as shown in Figure 3.9. For the data shown at a rotational rate of 1500 RPM in Figure 3.10 the frequency spectra of the baseline an serrated cases are virtually indistinguishable.

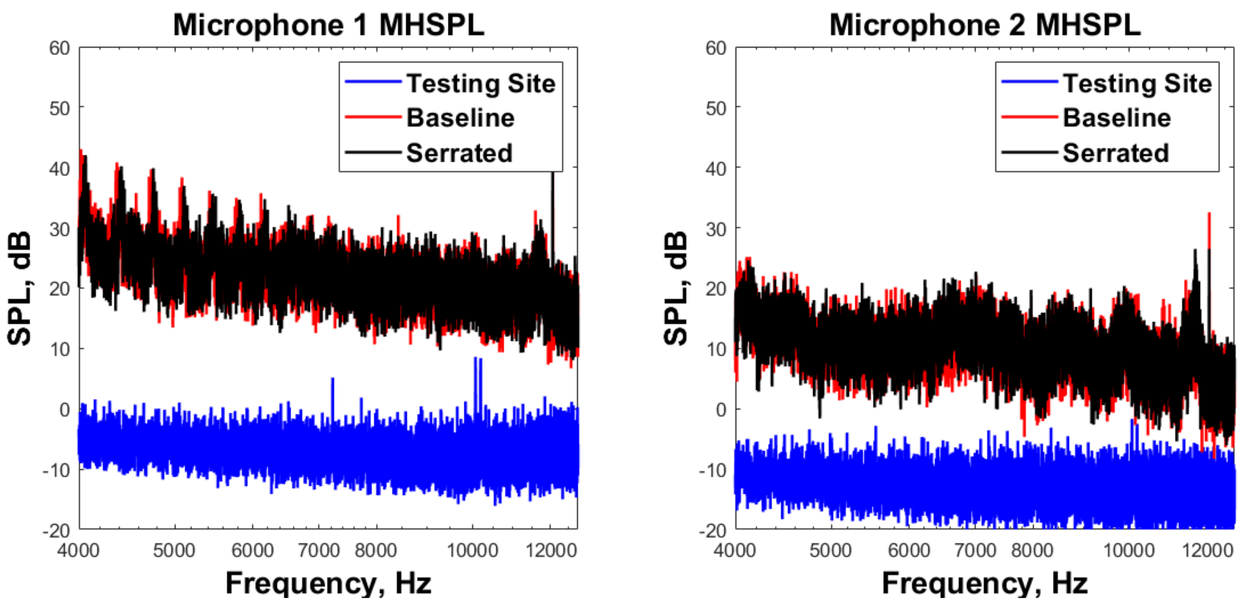

Figure 3.10: Comparison of middle-to-high frequency ranges for 10 degrees pitch angle for baseline and serrated blades at 1500 RPM

Table 3.1: Pitch Control OASPL Comparison

Parameter	Baseline	Serrated	Δ OASPL
OASPL	92.1 dB	91.2 dB	0.9 dB
MHSPL	60.1 dB	58.3 dB	1.8 dB

The overall sound reduction benefits at microphone 1 for rectangular blades at 2000 RPM are summarized in Table 3.1. These results confirm the hypothesis that more beneficial sound reduction is achieved when measuring in the frequency range of MHSPL when compared to the full audible frequency range. Coincidentally, the location of this range is fortuitous with respect to human hearing. This range from 4000 to 12800 Hz nears the peak of the A-weighting scale. This proximity would lead to increased benefits of reduced SPL in this range.

3.2.2 Acoustic Results for Coaxial Rotor with Twisted Blades

As this study progressed, the need for a more accurate model of a small-scale UAV became evident. While the small rectangular blades used in the first experimental setup were useful for preliminary tests, the majority of rotor blades used in modern UAVs have both a swept chord, as well as a pitch angle that varies from root to tip, known as twist. These blades provided unique aerodynamic as well as aeroacoustic characteristics.

The results shown in Figure 3.11 were acquired to compare both varying latitude angles as well as the single and double rotor data. This set of data was taken in the same plane as the blade crossing location, to highlight the interactions that are prevalent at this location in a coaxial rotor. Each set of azimuthal OASPL measurements was calculated by taking the average OASPL of five 10-second trials for each data point. The main highlight from this plot is that the variation between microphone measurements across latitude angle is noticeably smaller for the single rotor when compared to the double rotor case. This occurrence is most likely due to increased blade-vortex interaction noise.

Another notable feature of Figure 3.11 is the minimum and maximum the standard deviations (σ) noted for each of the azimuthal θ locations, which can be found in Appendix Tables A.1-A.8. These minimums and maximums denote the extremes across the entire array of latitude angles. While the maximum standard deviations are higher than expected, they were all found for microphones in the downwash locations. Therefore, these microphones

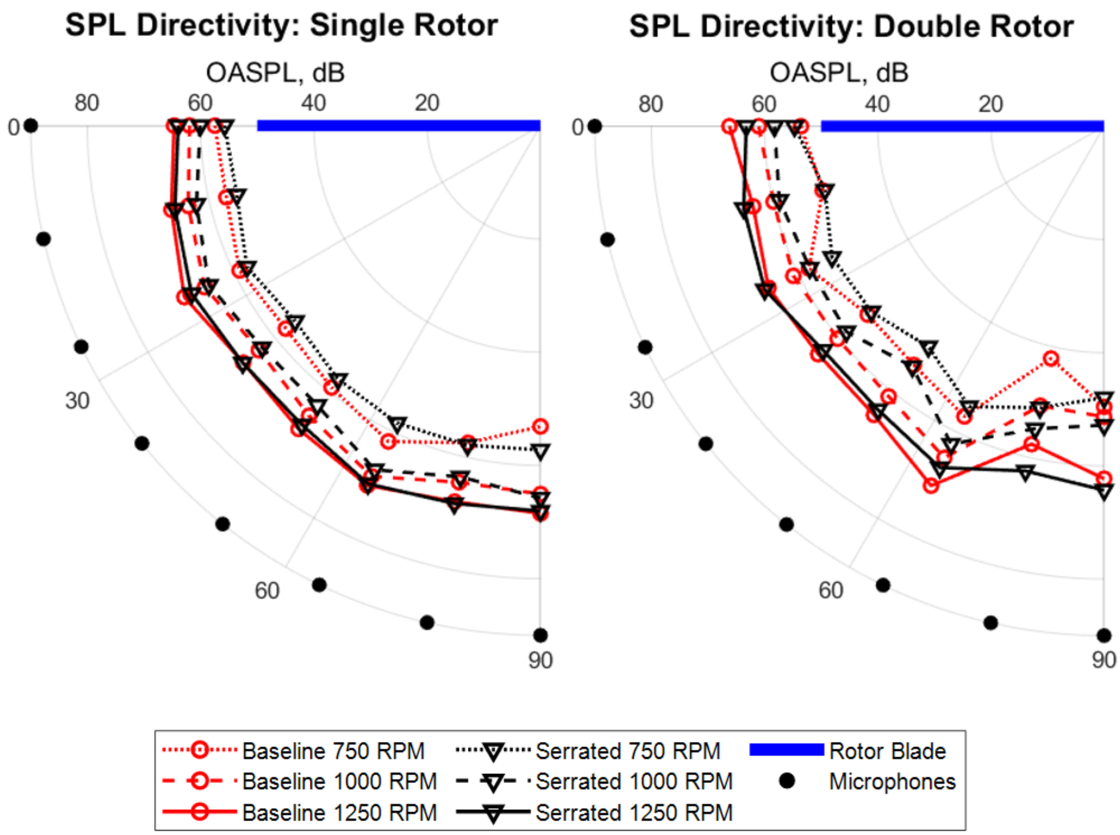

Figure 3.11: OASPL measurements for the twisted single rotor ($\sigma_{max} = 2.1$; $\sigma_{min} = 0.1$) and twisted combined coaxial counter-rotating rotor ($\sigma_{max} = 5.7$; $\sigma_{min} = 0.2$) at $\theta = 0^o$ for rotational rates of 750, 1000, and 1250 RPM. Individual data for each microphone shown in Appendix Tables A.1-A.8

all experienced higher incoming velocities as well as increased vortex interactions. Both of these conditions can lead to increased pressure fluctuations and therefore, a higher deviation in sound pressure measurements. This same effect of increased deviation in sound pressure is shown in Figure 3.12 for the remaining three θ locations.

All double rotor acoustic tests were run for 4 different azimuthal angles of θ which can be seen in Figure 2.7b. This range of angles was chosen as the blade crossing location occurs every 90 degrees in a two-bladed coaxial counter-rotating rotor setup. Half of this rotational span covers the majority of the blade interactions present.

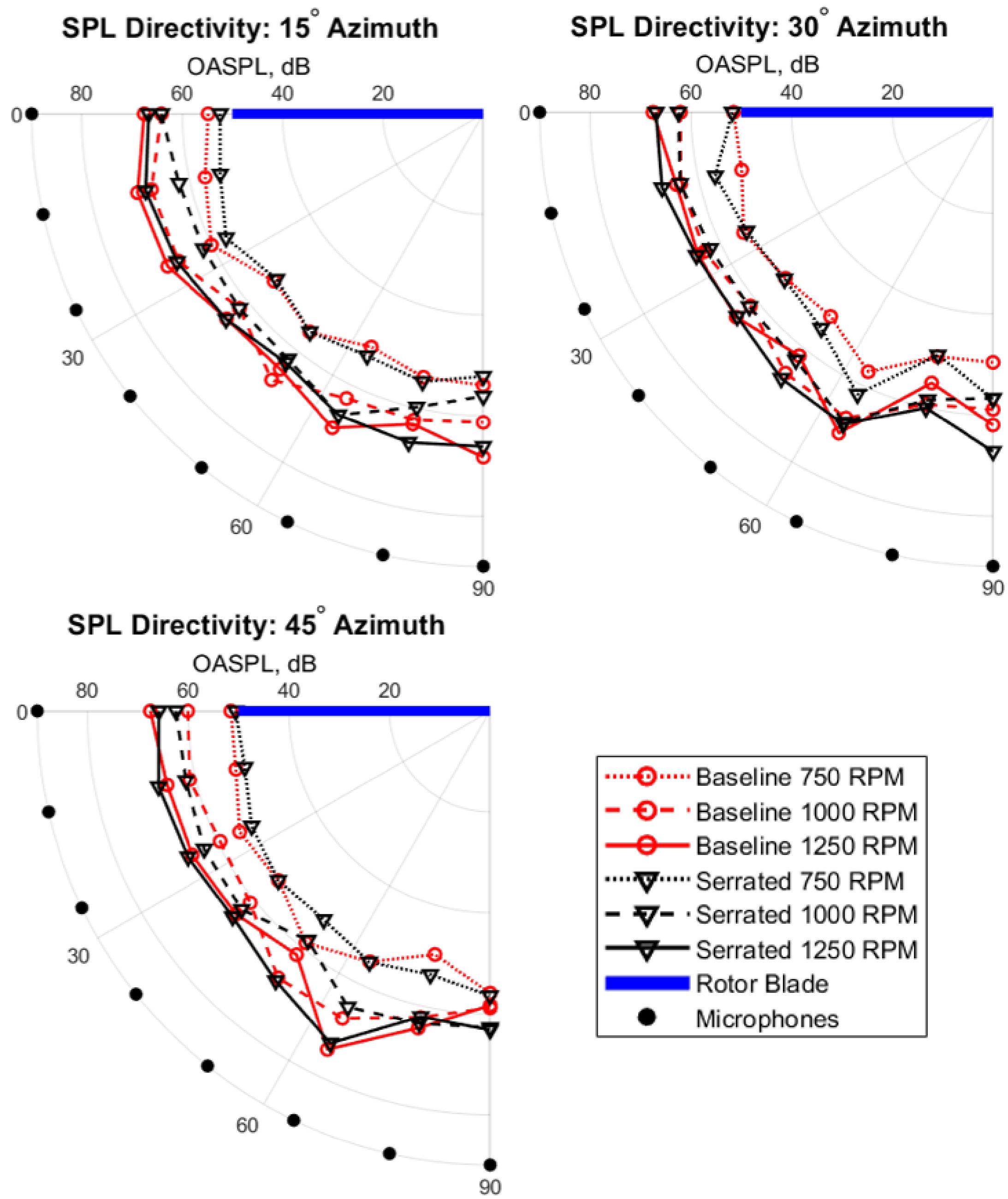

Figure 3.12: OASPL measurements for the twisted blades coaxial counter-rotating rotor at $\theta = 15^o$ ($\sigma_{max} = 9.7$; $\sigma_{min} = 0.3$), $\theta = 30^o$ ($\sigma_{max} = 7.2$; $\sigma_{min} = 0.1$), and $\theta = 45^o$ ($\sigma_{max} = 9.9$; $\sigma_{min} = 0.3$) azimuth angle for rotational rates of 750, 1000, and 1250 RPM. Individual data for each microphone shown in Appendix Tables A.1-A.8

The first azimuthal angle next to the blade crossing location that was analyzed was the $\theta = 15^o$ degree location. This data shown in Figure 3.12, shows the unique acoustic interactions present 15^o past the blade crossing location. From a cursory viewing of the plot at $\theta = 15^o$, it is evident that the OASPL varies within a smaller margin across latitude angles when compared to the blade crossing location. While the variation between the individual cases is smaller, the benefit of serrations is much larger for certain latitude angles. This benefit is shown to be maximized for microphones one, two, and three at a rotational rate of 1000 RPM, with microphone three showing a reduction in 6 dB. This location would most likely be associated with the presence of blade vortex interaction and thickness noise. In addition, a reduction in the amplitude of the blade crossing could effect these microphones as they lie closest to the blade tips. Lesser benefits are shown for both the higher and lower rotational rates. Similar performance, and even and increase in the serrated case was observed for lower latitude angles at this azimuthal angle, suggesting the absence of reduction in loading noise.

Progressing to the next azimuthal angle at $\theta = 30^o$ past the blade crossing location, another unique set of interactions is present. The mean OASPL level and lack of benefit from the addition of serrations remains constant aside from the last two microphone locations. At microphones 7 and 8 the OASPL drops by approximately 10 dB when compared to neighboring values of ϕ. This drop in OASPL could be explained by the region directly below the center of the rotor being absent of tip vortices as well as any direct noise sources other than loading noise. No significant or distinct reduction in OASPL between the baseline and serrated cases can be noted from the $\theta = 30^o$ azimuthal angle.

At the next azimuthal angle of $\theta = 45^o$, the midpoint between two blade crossing locations is captured. This location, similar to other azimuthal measurement points is very important as the interactions present here are likely to be replicated at 3 other points over the course of a single revolution of a coaxial counter-rotating rotorcraft. Similarly, these interactions would occur more frequently as the number of blades increases. In the data shown for the $\theta = 45^o$ azimuth angle, similar phenomena to the $\theta = 30^o$ azimuth angle is evident in the greater angles of ϕ at the lower half of the hemisphere. As the angular location of the microphone increases, the OASPL at 750 and 1000 RPM steadily decrease, reaching a minimum directly below the shaft of the rotor.

Similarly to Figure 3.11, the standard deviation of each of the three cases shown in Figure 3.12 were higher than expected. After closer examination of the standard deviation in each of the microphones, shown in Tables A.1-A.8, it was discovered that the highest standard deviation values were consistently found at microphones six, seven, and eight. The locations of these microphones correspond with the area directly below the rotor where the downwash is located. In addition, the highest single standard deviation for most cases was found at microphone six, where the free shear layer between the downwash and the neighboring quiescent flow is located. This location would also coincide frequently with trailing tip vortices.

In addition to OASPL measurements, Fourier transforms of the acoustic signals were assessed in order to visualize the variance of sound pressure level with frequency. Sound pressure measurements shown relative to frequency include, by nature, a significant amount of noise. In order to mitigate extraneous noise in the signals shown, the average from 5 test trials are presented. The data shown in Figure 3.13 displays this averaged signal for 5 test trials as well as the sequential averaging of the coaxial counter-rotating rotor at 1250 RPM. For each of these plots, the baseline and serrated cases are shown. Variations in these plots were observed to display the largest variations between baseline and serrated cases in the higher frequency ranges. Measurements were also taken for rotational rates of 750 and 1000 RPM, however this data did not display noticeable variation between the baseline and serrated cases aside from the blade passing frequency.

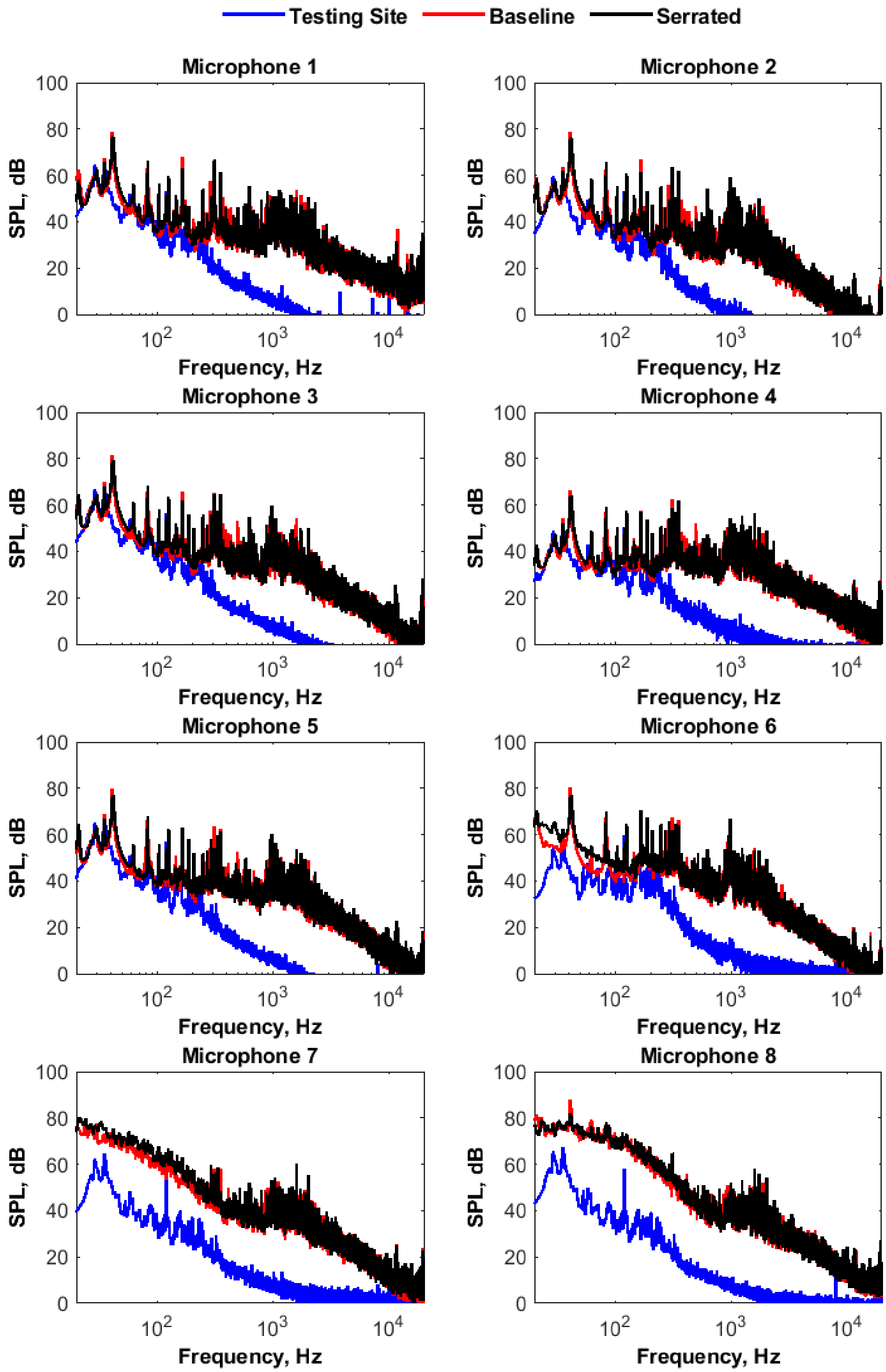

Figure 3.13: Averaged Fourier Transform of acoustic signal from 20 to 20,000 Hz at 1250 RPM for serrated and baseline rotor blades

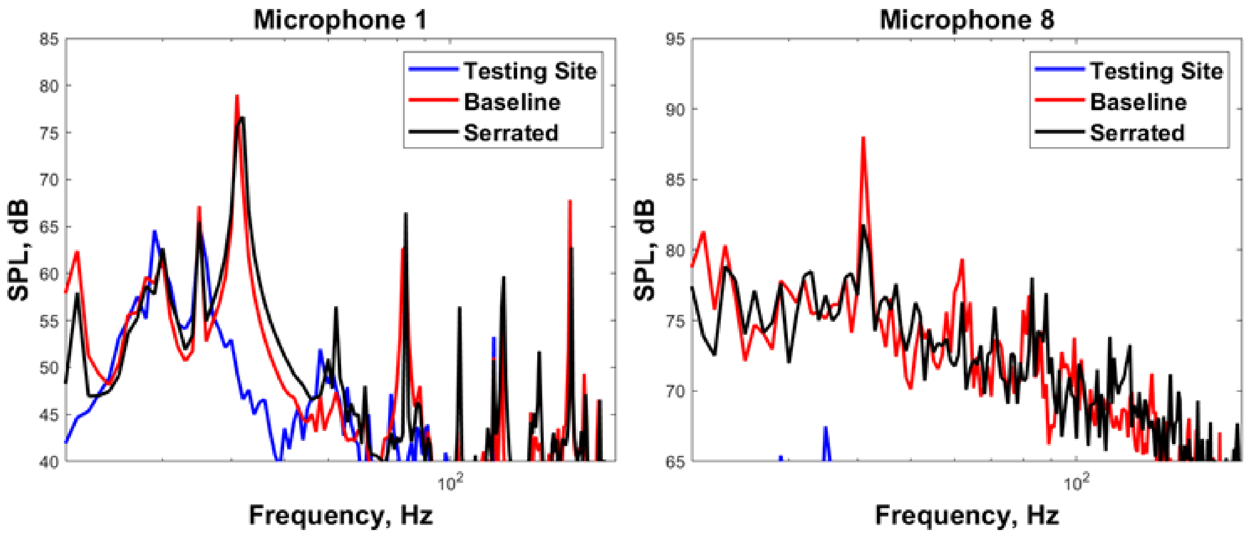

(a) (b)

Figure 3.14: Close-up view of the blade crossing frequency at 1250 RPM for (a) Microphone 1 (b) Microphone 8 for the twisted blade coaxial rotor

The most prominent feature of Figure 3.13 is the blade crossing frequency located at 41.67 Hz, for this case of 1250 RPM. In Figure 3.14, the area near blade crossing frequency is shown in more detail. The reduction in amplitude of blade crossing frequency is positive for every microphone at these operating conditions. The specific reductions in blade crossing frequency amplitude for microphones one and eight are 3 dB and 7 dB, respectively. This reduction is most likely caused by the process of spectral broadening of the main tonal frequency. In this scenario, the blade crossing frequency is twice that of the blade passing frequency of a single rotor system rotating at the same rotational rate. This frequency spike is easily identifiable as the highest peak for any angle of ϕ. In addition, the harmonic frequency at 83.33 Hz is also identifiable, however, a difference between the baseline and serrated frequency at this point was not beneficial.

Another prominent feature of Figure 3.14 is the difference in low frequency profile of microphone eight compared to that of microphone one. The frequency plot of microphone eight shows that the blade crossing frequency has been muddled by surrounding frequencies. This is thought to be the result of the high-speed downwash flow at this microphone's location and is commonly known as "rumble". This rumble is caused by the direct collision of incoming fluid on the diaphragm of the microphone, causing increased fluctuations in dynamic pressure.

Table 3.2: Summary of OASPL for Twisted Blade Experiments

Configuration	RPM	Baseline Avg.	Serrated Avg.	Δ OASPL
Single Rotor	-	-	-	-
	750	57.8 dB	56.8 dB	-1.0 dB
	1000	64.9 dB	63.8 dB	-1.1 dB
	1250	68.0 dB	67.5 dB	-0.5 dB
Double ($\theta = 0°$)	-	-	-	-
	750	54.6 dB	55.3 dB	0.7 dB
	1000	61.2 dB	61.1 dB	-0.1 dB
	1250	67.6 dB	66.6 dB	-1.0 dB
Double ($\theta = 15°$)	-	-	-	-
	750	55.0 dB	53.9 dB	-1.1 dB
	1000	64.5 dB	62.0 dB	-2.5 dB
	1250	67.4 dB	66.5 dB	-0.9 dB
Double ($\theta = 30°$)	-	-	-	-
	750	51.1 dB	53.6 dB	2.5 dB
	1000	63.1 dB	62.0 dB	-1.1 dB
	1250	64.3 dB	66.2 dB	1.9 dB
Double ($\theta = 45°$)	-	-	-	-
	750	52.4 dB	51.4 dB	-1.0 dB
	1000	59.4 dB	61.3 dB	1.9 dB
	1250	65.0 dB	63.2 dB	-1.8 dB

The data shown in Table 3.2 is a combination of all average OASPL values taken for the single and coaxial counter-rotating rotors across all 8 microphones for the coaxial rotor with twisted blades. This table reveals how noise reduction due to blade modification varies when compared against azimuth angle θ. This table also shows that while single rotors show consistent benefit from trailing edge serrations, coaxial counter-rotating rotors benefit greatly in some directivities, while others do not benefit at all. This lesser benefit shown for the coaxial counter-rotating case could be a result of the increased turbulent interactions between two rotors as shown in previous literature [33]. In the last column of this table the overall change in OASPL is given in green if the addition of serrations reduced the noise and red if it did not reduce the noise produced.

3.3 Velocity Field Results for Coaxial Rotor with Twisted Blades

As testing on this blade modification study progressed, a need for a physical understanding of the flow mechanisms being manipulated became evident. The most useful and easily accessible method to measure these flow mechanisms was through the use of PIV. The area of interest in this study was the downwash area below the lower rotor of the double rotor setup. This area was divided into two sections as shown in Figure 2.11. The upper frame, shown in red, was used to observe interactions in the adjacent downwash area. The second area, shown in blue, was mainly used evaluate the magnitude of the turbulence intensity far below the rotor.

3.3.1 PIV Scalar Fields

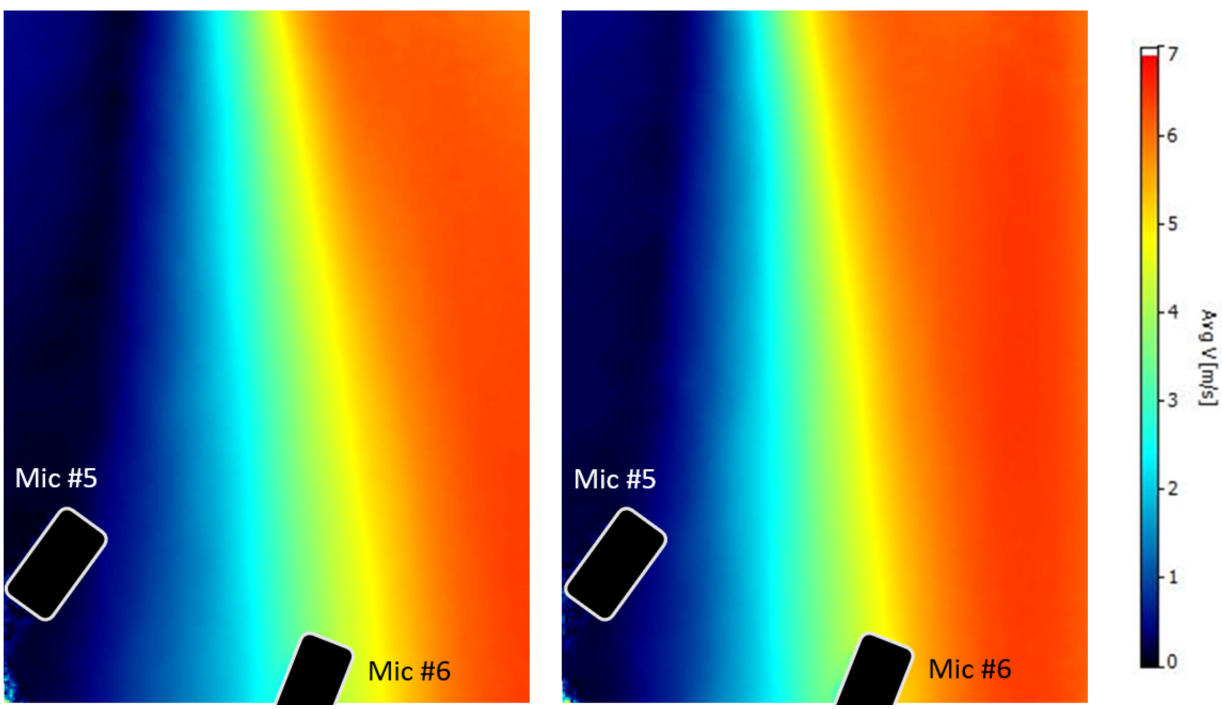

Figure 3.15: Velocity magnitude of the twisted blades for baseline (left) and serrated (right) at downstream location at 1250 RPM. Microphone 6 is shown in this downwash location

After an isolated acoustic analysis was performed on the coaxial rotor, the qualitative flow fields were analyzed. These flow fields are presented in the form of scalar velocity magnitude plots. This flow field analysis was completed in order to connect physical mechanisms of aeroacoustic noise to the acoustic measurements made previously.

The velocity fields shown in this section are all time-averaged flow field images which represent the average velocities at each point in the field of view over the time allotted. In these test cases, each data acquisition period was 2000 frames. The scalar field color represents the velocity magnitude for any given point. The first two images shown in Figure 3.15 display the lower frame in both the baseline (left) and the serrated (right) cases. A recurring difference between the two cases is the magnitude of the velocity gradient moving from the center of the rotor outwards radially. The increased width of the serrated downwash could be attributed to increased turbulence and mixing in the near field due to the serrations

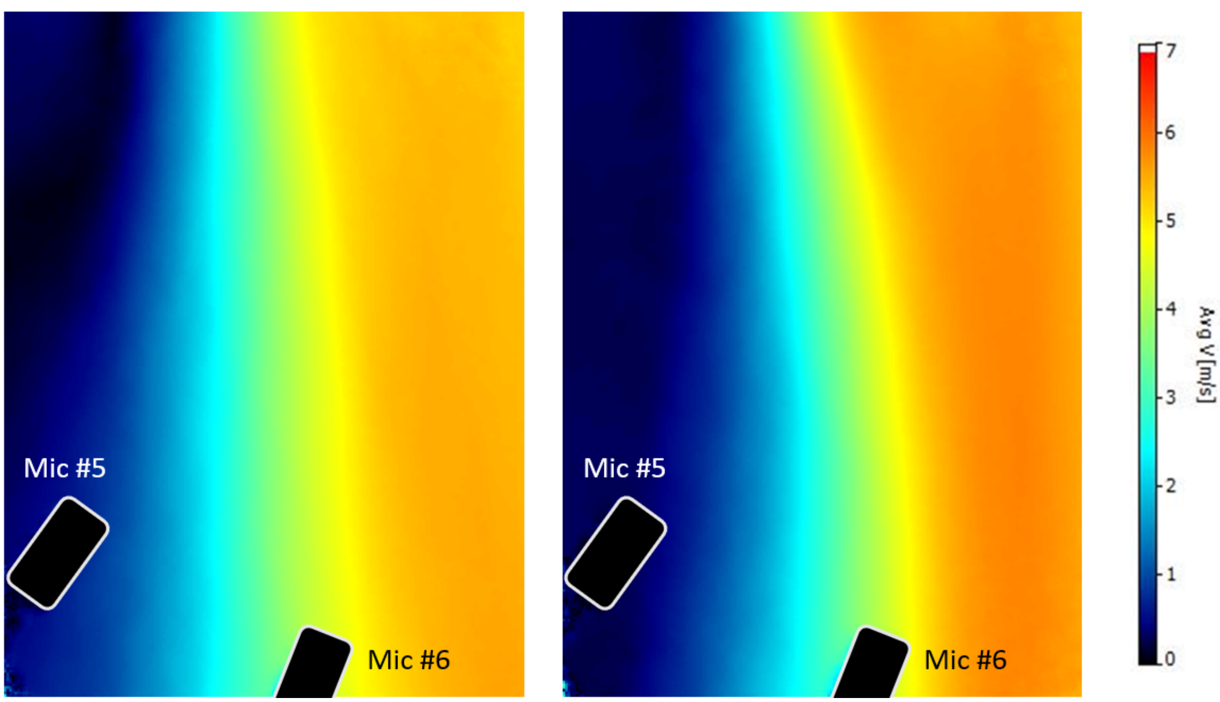

Figure 3.16: Velocity magnitude of the twisted blades for baseline (left) and serrated (right) at downstream location at 1000 RPM. Microphone 6 is shown in this downwash location

The difference in gradient seen in the lower field of view continues through Figure 3.16 in the case of 1000 RPM for the same PIV frame. This variation in wake contraction rate and downwash size has been found in past studies as well [34]. In this literature study it was concluded that rotor blades with trailing edge serrations cause an increase in the average speed of flow in the center of the downwash, and consequently, an increase in the rate at which the velocity decreases as the location moves outward.

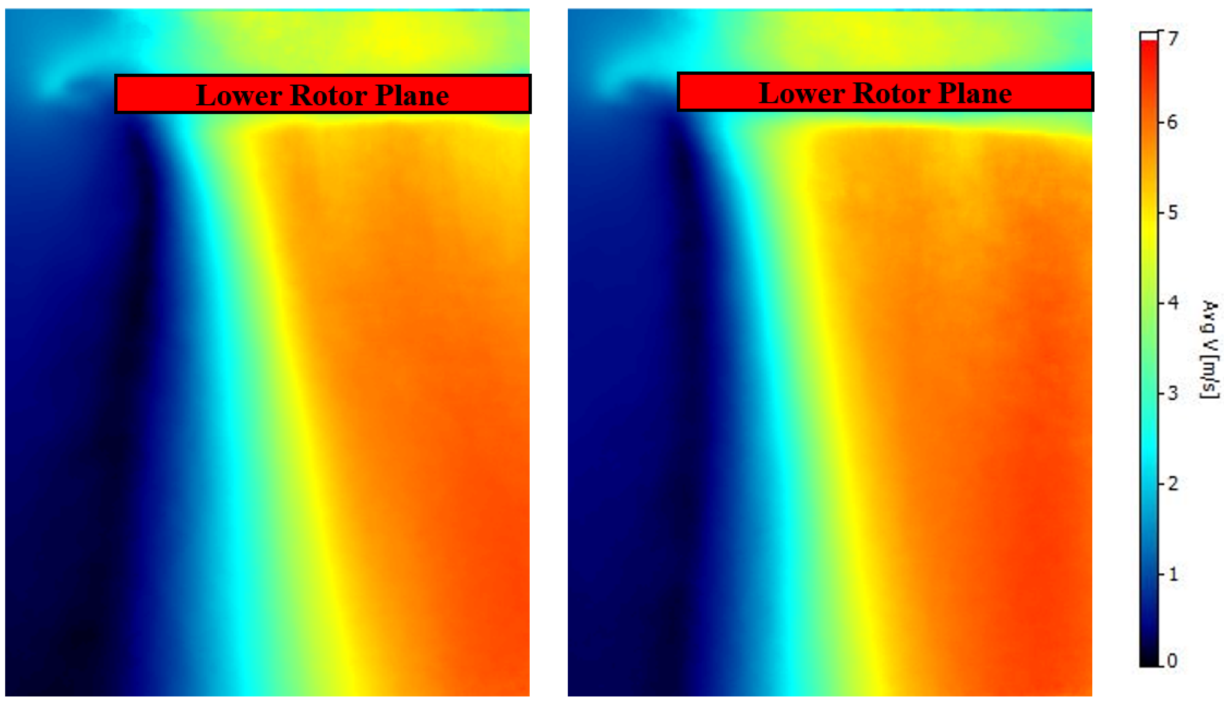

Figure 3.17: Velocity magnitude of the twisted blades for baseline (left) and serrated (right) at upstream location near rotor planes at 1250 RPM

Moving upward toward the rotor, Figure 3.17 shows the upper frame of the time-averaged flow field for an RPM of 1250. In this frame the position of the lower rotor plane is visible. A similar phenomena in downwash size and velocity gradient is visible at the lower part of the image. This discrepancy in gradient between the scalar values of 1 and 5 meters per second on the color gradient is clearly visible when comparing the baseline and serrated figures.

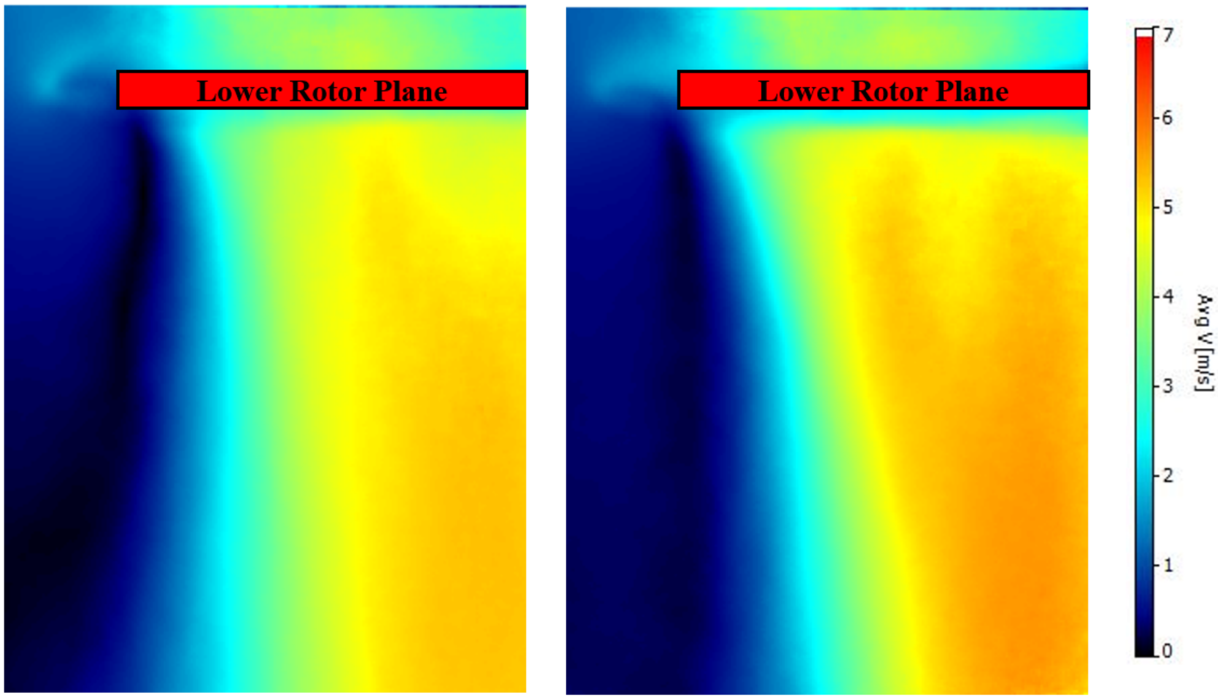

Figure 3.18: Velocity magnitude of the twisted blades for baseline (left) and serrated (right) at upstream location near rotor planes at 1000 RPM

In a similar comparison, Figure 3.18 shows the data taken at a rotational speed of 1000 RPM. The same phenomena is visible to a lesser extent as the velocities involved are lesser on average. Overall, the velocity fields shown in this section support the notion that the addition of trailing edge serrations causes a significant and noticeable difference in the downwash region below the rotor. However, more analysis is required in order to tie this change in flow field characteristics to the previously identified reduction in OASPL.

3.3.2 Velocity Profiles

The diagram shown in Figure 2.11 maps out the 5 horizontal locations at which velocity profiles were analyzed. The distances shown are relative to the lower rotor plane. Levels in between the two rotor planes were not shown as the flow field was not easily discernible from the blades themselves. Velocity profiles below 17 cm (0.34D) were determined to be unnecessary as the main flow characteristics were identified above this point. All velocity profile data was extracted directly from the field of velocity magnitude values, by taking a single horizontal line of values for each of the downwash levels.

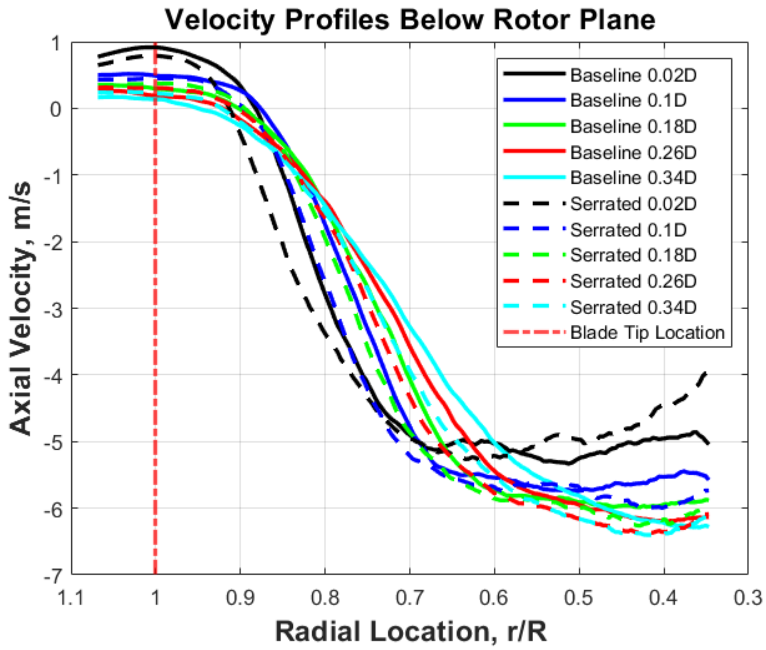

Figure 3.19: Velocity profile for all distances below the rotor plane for the baseline and serrated cases including the blade tip location

In the velocity profile plot, shown in Figure 3.19 the velocity profiles are shown for each level below the rotor plane with respect to radial location. This figure clearly shows the development of the downwash region as the maximum velocity becomes more consistent. The transition from high to low gradient of the baseline profiles and the opposite transition from low to high gradient of the serrated profiles show that there are definite and measurable differences in the two flow fields.

The first velocity profile shown is displayed in Figure 3.20. This plot shows the variation of velocity magnitude with radial location, with the rotor tip marked as a vertical line. At 0.1D below the rotor plane, the velocity profile is still in an unsteady state towards the center of the rotor, and is far from fully-developed. The most notable features that are visible in this figure are the differences in location of maximum velocity as well as the difference in the gradient from low to high velocity. At this point in the flow, the maximum gradient of the

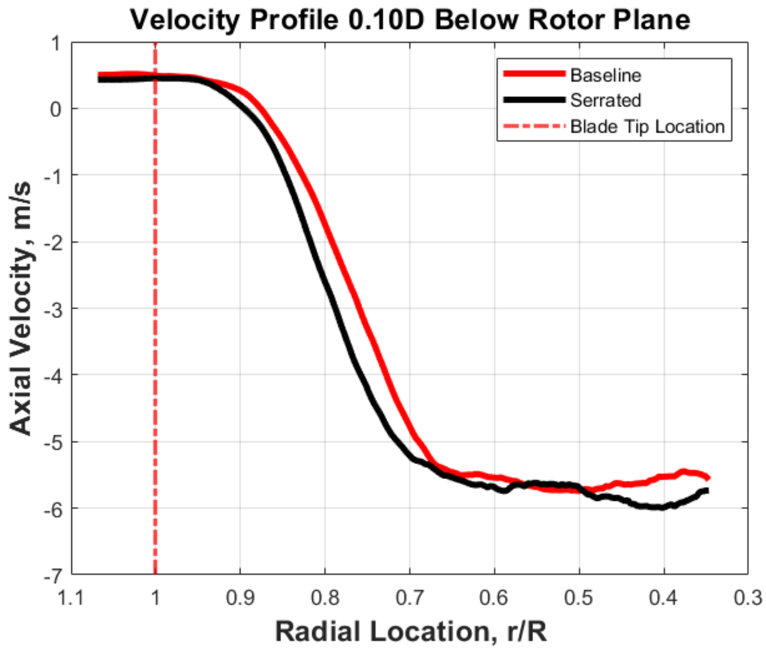

Figure 3.20: Velocity profile 1 cm (0.02D) below the rotor plane for the baseline and serrated cases including blade tip location

serrated case is greater than that of the baseline case. This data proves that the trend of an increased spread of the downwash carries over from single rotors shown in previous studies to the current coaxial rotor [34].

At the location 0.34D below the rotor plane, the progression from root to tip location is more reminiscent of a fully developed flow. In Figure 3.21 the maximum gradient of the serrated case is now greater than that of the baseline case, suggesting a quicker transition and a higher gradient between the downwash cylinder and the neighboring quiescent flow.

In addition to this higher gradient found further below the rotor, there are quantifiable differences in the maximum velocity for each of the cases in Figure 3.21. The maximum velocity for the field of view that was studied was larger in the serrated case when compared to the baseline case. This greater velocity would cause and increase in dynamic pressure incident on the lower microphones which could lead to a higher OASPL readings for the serrated case. This higher velocity for the serrated case provides an explanation for the negative reduction in OASPL for microphones seven and eight in Figures 3.11 and 3.12.

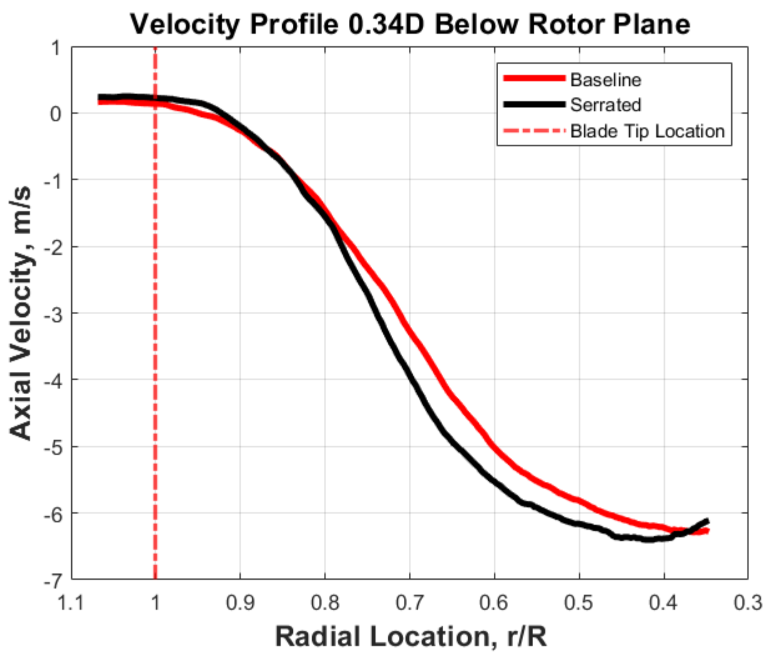

Figure 3.21: Velocity profile 17 cm (0.34D) below the rotor plane for the baseline and serrated cases including blade tip location

While these velocity profiles provided insight into some of the acoustic interactions found, there is even more that can be done to dissect the previously found velocity fields.

3.3.3 Turbulence Intensity

A main factor that is thought to decrease the production of tonal frequencies in the downwash of a small rotorcraft is increasing the turbulent mixing in the flow field. The addition of serrations to the trailing edge if though to promote this turbulence and could therefore increase the mixing of the trailing flow field. This increase in turbulent mixing in the early downwash could lead to a faster decay in overall turbulence intensity and subsequently, less turbulence induced noise in the far-field.

In Figure 3.22 the turbulence intensity has been extracted from the plane 0.1D below the lower rotor plane. After taking the integrals of each of the turbulence intensity functions, it was determined that there was a 9.6 percent increase in the turbulence intensity in the serrated case when compared to the baseline case.

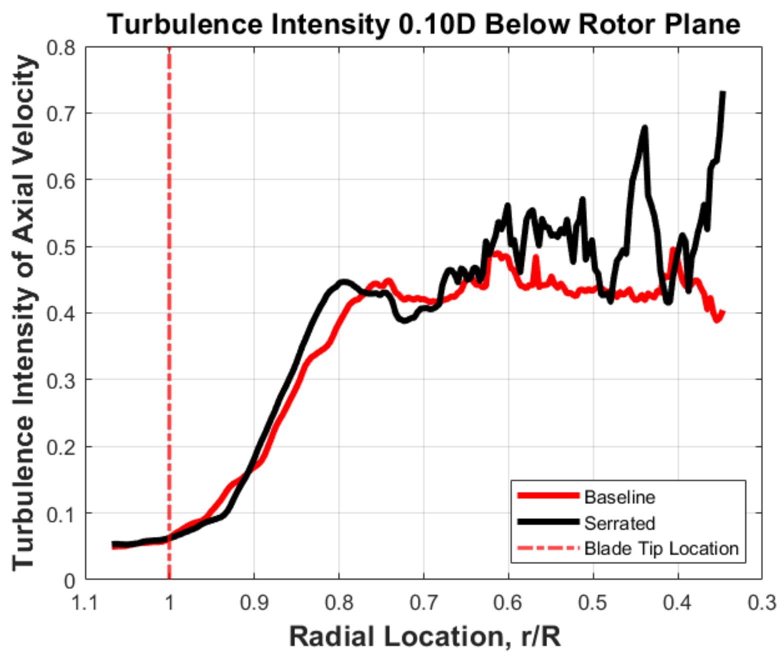

Figure 3.22: Turbulence intensity at 5 cm (0.10D) below the rotor plane for the baseline and serrated cases including the blade tip location

As the flow field progresses downstream, the turbulence intensity evolves similarly to the velocity profiles. At at a point 0.34D below the rotor plane shown in Figure 3.23 the difference in integrals between the two rotor cases has become much less. The total turbulence intensity at this location was 1.5 percent higher for the baseline case when compared to the serrated case. This difference implies a reversal of turbulence intensity dominance somewhere in between these two downwash locations.

Furthermore, at a level 0.5D, shown in Figure 3.24, the turbulence intensity comparison further diverges, as the difference in total turbulence intensity for the serrated case is 3 percent less than the baseline case. This decrease in turbulence intensity for the serrated in comparison to the baseline case would usually imply a decrease in OASPL in the far-field locations, however, this decrease is not shown. Rather, ad increase is in OASPL was shown for the serrated case was shown. This leads to the conclusion that turbulence intensity-based noise sources are not the dominate noise production mechanism at the downstream location.

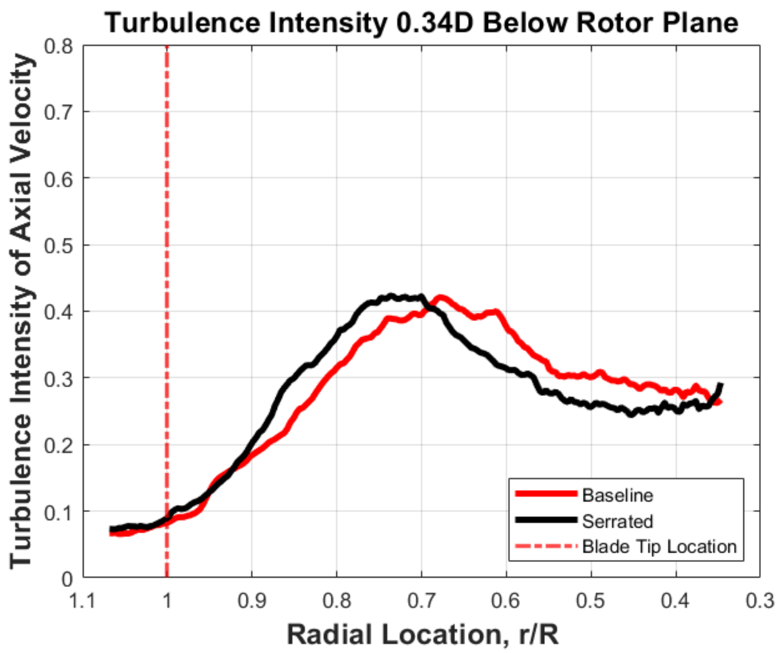

Figure 3.23: Turbulence intensity at 17 cm (0.34D) below the rotor plane for the baseline and serrated cases including the blade tip location

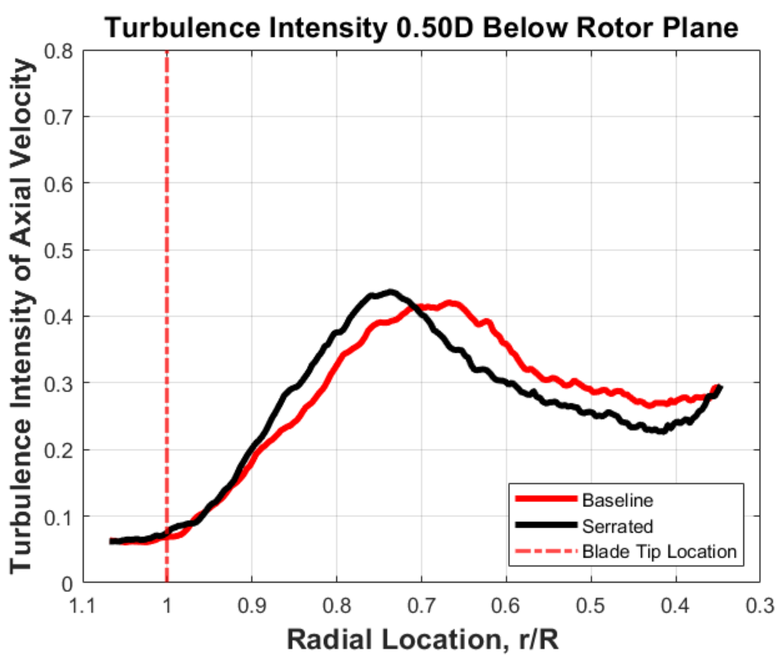

Figure 3.24: Turbulence intensity at 25 cm (0.50D) below the rotor plane for the baseline and serrated cases including the blade tip location

Chapter 4

Concluding Remarks

In this study the aerodynamics and aeroacoustics of a counter-rotating coaxial rotor were compared to those of a single rotor while using both a regular (baseline) blades as well as blades with the addition of a sawtooth serrated trailing-edge. This blade modification was chosen due to its success in past studies. This success refers to the ability of a blade with trailing-edge serrations to reduce the OASPL produced by a single rotor, while leaving the aerodynamic performance virtually unaffected. The two main conclusion objectives are stated in a manner similar to the two main objectives outlined in the introduction.

1. **Objective 1**: Quantify the aerodynamic effects of trailing-edge serrations on a coaxial rotor in hover

   (a) The aerodynamic comparisons made through thrust and torque measurements in this study found minor differences between the baseline and serrated cases. These differences mainly appeared at lower rotational rates and pitch angles. The overall similarity in aerodynamic performance between the two cases can be attributed to the design of the 3D printed rotor blades, and their equality in planform area. The relevance of any differences present in trends of thrust and torque were reduced by identifying the conditions that displayed minimal discrepancies. These selected conditions were then used to acquire acoustic data.

   (b) The axial flow below the rotor was quantified using PIV measurements. The findings from these measurements revealed that a higher velocity gradient exists in wake contraction of a serrated rotor compared to a baseline rotor. This increased gradient caused the downwash region to contract to a greater extent in the serrated case. This contraction also proves that a higher velocity is found in the center of the downwash below the serrated rotor. The turbulence intensity derived from these velocity measurements also provided the insight that a faster rate of decay in turbulence intensity is present for the serrated case when compared to the baseline case.

2. **Objective 2**: Collect acoustic data and identify connections to aerodynamic data

   (a) Through the analysis of these OASPL results, collected for 8 different latitude angles of ϕ as well as 4 different azimuth angles of θ, it was determined that the reduction in OASPL of a coaxial rotor is highly dependent on the latitude and azimuth location, which denote different aerodynamic sources of noise. Furthermore, the OASPL and total reduction in OASPL is more consistent across latitude angles for a single rotor when compared to a coaxial counter-rotating rotor. Despite this inconsistency, a benefit of serrations for a coaxial counter-rotating rotor was found for higher hemispherical latitude angles.

   (b) The frequency spectra across different rotational rates were analyzed as well. In the frequency range associated with MHSPL the noise attenuation was seen to increase for a rectangular fixed-pitch blade, but not for a twisted rotor blade. However, it is hypothesized that the addition of serrations increases the accumulation of turbulent structures which led to lower peaks in FFT measurements, especially at blade passing frequency. This phenomenon was identified as spectral broadening, where the peaks are reduced and neighboring amplitudes are increased as a reaction.

   (c) The PIV analysis was achieved by connecting each observed sound to a theoretical source of rotorcraft noise. First, the reduction in OASPL at higher hemispherical latitude angles can be associated with blade-vortex interaction noise or thickness noise, corresponding to quadrupole or monopole noise sources. Second, the increase in OASPL for the serrated case at the lowest hemispherical latitude angles near microphones seven and eight, are tied to an increase in dipole loading noise in this same area. This theory was confirmed by the higher velocity measurements in the serrated case for the lower velocity profile locations. The faster rate of decay in turbulence intensity for the serrated case would usually suggest a lower OASPL in the far-field measurements. Unfortunately, this decrease in turbulence far below the rotor did not lead to a decrease in OASPL at the corresponding location. However, this finding leads to the conclusion that the noise produced directly below the rotor is not dominated by turbulence-based noise sources.

The work in this study was used to analyze improvements made to current UAV rotor blades. This study utilized two experimental rotor test stands in order to evaluate the acoustic and aerodynamic characteristics of rotor blades with two trailing-edge designs. Together, the methods utilized were able to determine the quantitative differences in the OASPL, frequency spectra, and axial flow fields between the two rotor blade cases.

While the results shown in this study were gathered from a focused set of experiments, the implications of such results are much more broad. In this study it was shown that with minor modifications to a rotor blade, a measurable difference in the sound produced was achieved while presenting minimal differences in aerodynamic performance. Specifically, a coaxial counter-rotating rotor with trailing-edge serrations that presents numerous flow interactions absent in a single rotor configuration, produces both positive and negative differences in the resulting acoustic signature, depending on directivity location. With this knowledge, the future of quieter, and therefore more effective rotorcraft is more feasible.

Chapter 5

Future Work

While the current twisted blades coaxial test stand provides many opportunities to collect data from altered experimental conditions such as new blade modifications or PIV configurations, there are also opportunities for further analysis of the current flow field data. Specifically, the temporal frequency of specific points in the velocity flow field could be analyzed to make more detailed connections between the flow field and the acoustic results. This analysis could be completed through the use of a fast Fourier transform of the velocity data at a single point in the downwash. It is possible that prominent frequencies found in the acoustic data could be correlated to similar frequencies identified in the flow field Fourier transform.

As it was discussed in the background section of this thesis, there have been a variety of studies in the past that have focused on different methods of sound attenuation caused by rotor blade modifications. This study focused on extrapolating one of these single rotor methods to the coaxial counter-rotating case. This same type of extrapolation could be applied to many other blade modifications.

One additional blade modification that has shown promise in past studies is the method of tip modification. This method has been implemented on thousands of commercially manufactured small UAVs. The logical next step in this study would be to expand the current instrumentation and coaxial rotor setup to blades with swept tip modifications.

Another step that could be taken in the future is to examine the flow interactions in between the two rotors. Since this region is non-existent in the single rotor case, it has not been studied in detail for the coaxial counter-rotating case with tip modifications or serrated trailing-edges. More specifically, this will help address the observed decrease in SPL during blade passage due to the introduction of serrations on the blade's trailing edge. A PIV configuration that could achieve this goal is shown in Figure 5.1.

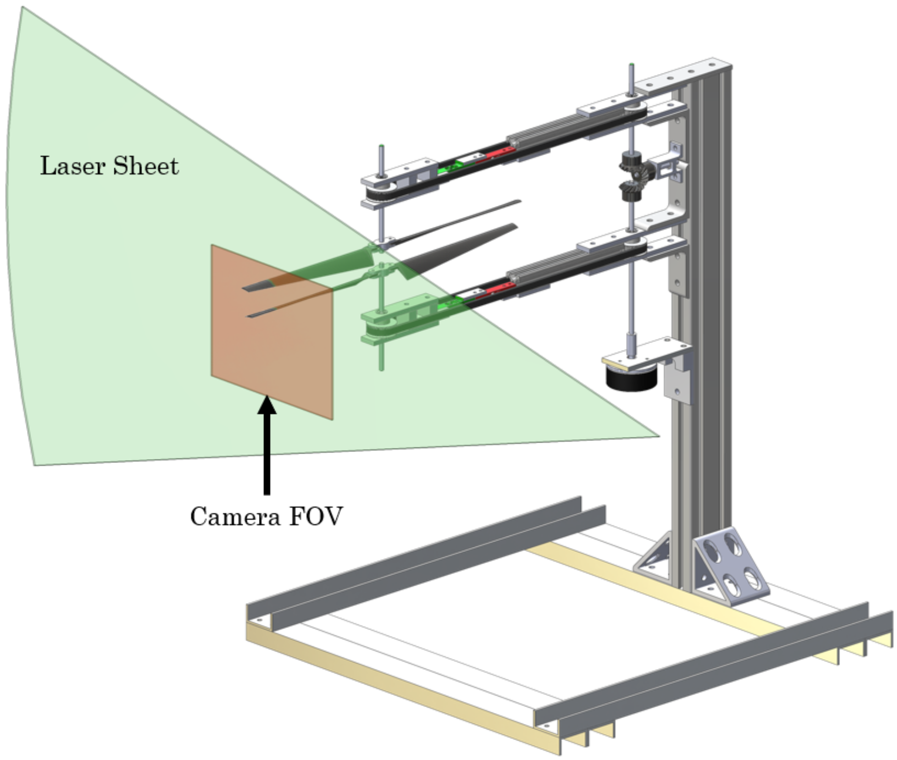

Figure 5.1: Chord-wise PIV configuration

While the first set of PIV experiments yielded useful data that revealed measurable differences in the downwash as well as the speed of wake contraction, they were unable to provide detail on the small interactions that occur between two serrated blades in a coaxial arrangement. These interactions could provide insight into the increases in loading dipole noise observed in this study. This secondary set of PIV experiments could be carried out to fill in these gaps.

Analog filtering is another tool that could prove to be beneficial to the results of further experimentation. As it was discussed previously, the high-pass filtering available on the acoustic amplification system was not utilized. This decision was made in order to preserve all active ranges of frequency in the audible range. In addition, the high-pass filtering available on the amplification unit was bounded by a small range (25-250 Hz). In future tests, the addition of an independent analog filtering system with more sophisticated filtering options such as an elliptic filter that can eliminate low-frequency noise while preserving important ranges that include information such as blade crossing/passing frequencies could be implemented.

Bibliography

[1] O'Donnell, Shea. "A short history of unmanned aerial vehicles." Media Centre Blog, Jun 16 (2017).

[2] Joshi, Divya. "Exploring the latest drone technology for commercial, industrial and military drone uses." Business Insider 13 (2017).

[3] Occupational Safety and Health Administration. "OSHA fact sheet: Laboratory safety noise." Washington, DC: OSHA (2011).

[4] Atmaca, E., I. Peker, and A. Altin. "Industrial noise and its effects on humans." Polish Journal of Environmental Studies 14.6 (2005).

[5] "Expanding the Envelope for Future Vertical Lift," S-97 Raider Demonstrator, Lockheed Martin, 2019.

[6] Yang, Yannian, et al. "Aeroacoustic and aerodynamic investigation of multicopter rotors with serrated trailing edges." 25th AIAA/CEAS Aeroacoustics Conference. 2019.

[7] Nallasamy, M., and Edmane Envia. "Computation of rotor wake turbulence noise." Journal of Sound and Vibration 282.3-5 (2005): 649-678.

[8] Williams, JE Ffowcs. "Aeroacoustics." Annual Review of Fluid Mechanics 9.1 (1977): 447-468.

[9] Russell, Daniel A., Joseph P. Titlow, and Ya-Juan Bemmen. "Acoustic monopoles, dipoles, and quadrupoles: An experiment revisited." American Journal of Physics 67.8 (1999): 660-664.

[10] Brentner, Kenneth S., and Feridoun Farassat. "Modeling aerodynamically generated sound of helicopter rotors." Progress in Aerospace Sciences 39.2-3 (2003): 83-120.

[11] "Aircraft Noise Issues," Federal Aviation Administration, United States Department of Transportation, Jan. 9, 2018.

[12] Tinney, Charles E., and Jayant Sirohi. "Multirotor drone noise at static thrust." AIAA Journal 56.7 (2018): 2816-2826.

[13] Everest, F. Alton. "Master handbook of acoustics." (2001): 1714-1715.

[14] Shukla, Dhwanil, and Narayanan Komerath. "Rotor–duct aerodynamic and acoustic interactions at low Reynolds number." Experiments in Fluids 60.1 (2019): 20.

[15] Treuren, K. W. V., and Wisniewski, C. F. (November 19, 2019). "Testing Propeller Tip Modifications to Reduce Acoustic Noise Generation on a Quadcopter Propeller." ASME. J. Eng. Gas Turbines Power. December 2019.

[16] Rao, Chen, et al. "Owl-inspired leading-edge serrations play a crucial role in aerodynamic force production and sound suppression." Bioinspiration & biomimetics 12.4 (2017): 046008.

[17] Li, Y., et al. "Aerodynamic and Aeroacoustic Analyses of a UAV Propeller with Trailing Edge Serrations." Proceedings of ACOUSTICS. Vol. 7. No. 9. 2018.

[18] Ning, Zhe, Richard W. Wlezien, and Hui Hu. "An experimental study on small UAV propellers with serrated trailing edges." 47th AIAA Fluid Dynamics Conference. 2017.

[19] Oerlemans, Stefan, et al. "Reduction of wind turbine noise using optimized airfoils and trailing-edge serrations." AIAA journal 47.6 (2009): 1470-1481.

[20] Gur, Ohad, and Aviv Rosen. "Multidisciplinary design optimization of a quiet propeller." 14th AIAA/CEAS Aeroacoustics Conference (29th AIAA Aeroacoustics Conference). 2008.

[21] Avallone, F., et al. "Noise reduction mechanisms of sawtooth and combed-sawtooth trailing-edge serrations." Journal of Fluid Mechanics 848 (2018): 560-591.

[22] Jaron, Robert, et al. "Optimization of trailing-edge serrations to reduce open-rotor tonal interaction noise." Journal of Fluids Engineering 140.2 (2018).

[23] Howe, M.S. Aerodynamic Noise of a Serrated Trailing Edge. BBN Laboratories, 10 Moulton Street, Cambridge, Massachusetts. Journal of Fluids and Structures. 1991.

[24] Sinibaldi, Giorgia, and Luca Marino. "Experimental analysis on the noise of propellers for small UAV." Applied Acoustics 74.1 (2013): 79-88.

[25] Biedermann, Till. Czechkay, Pasquale. Geyer, Thomas. Kameier, Frank. Paschereit, Christian. "Effect of Inflow Conditions on the Noise Reduction Through Leading Edge Serrations," Dusseldorf University of Applied Sciences, AIAA Journal Vol. 57, September, 2019.

[26] Pierre, Richard. Maguire, Daniel. "The Impact of A-weighting Sound Pressure Level Measurements during the Evaluation of Noise Exposure," Noise-Con 2004. Baltimore, Maryland. 2004.

[27] Wieneke, Bernhard. "PIV uncertainty quantification from correlation statistics." Measurement Science and Technology 26.7 (2015): 074002.

[28] Sciacchitano, Andrea. "Uncertainty quantification in particle image velocimetry." Measurement Science and Technology 30.9 (2019): 092001.

[29] Silwal, Lokesh, Karlyle Munz, and Vrishank Raghav. "Development and validation of a thrust-scaled counter-rotating coaxial rotor to study interactional aerodynamics." AIAA Scitech 2019 Forum. 2019.

[30] Ramasamy, Manikandan. "Hover Performance Measurements Toward Understanding Aerodynamic Interference in Coaxial, Tandem, and Tilt Rotors," UARC-NASA Ames Research Center. Journal of the American Helicopter Society. 2015.

[31] Otsuka, Hikaru, and Keiji Nagatani. "Effect of Reynolds numbers of 10,000 to 100,000 on rotor blades of small unmanned aerial vehicles." 34th AIAA Applied Aerodynamics Conference. 2016.

[32] Deters, Robert W., Gavin Kumar Ananda Krishnan, and Michael S. Selig. "Reynolds number effects on the performance of small-scale propellers." 32nd AIAA applied aerodynamics conference. 2014.

[33] Barbely, Natasha L., Narayanan M. Komerath, and Luke A. Novak. A study of coaxial rotor performance and flow field characteristics. Georgia Institute of Technology Atlanta United States, 2016.

[34] Klimchenko, Vera, and Anya R. Jones. "An experimental study of the effects of winglets and serrations on the wake of a wind turbine." 53rd AIAA Aerospace Sciences Meeting. 2015.

Appendix A

Tables and Figures

Microphone #1 OASPL

Configuration	RPM	Baseline		Serrated		ΔOASPL
		μ, dB	σ, dB	μ, dB	σ, dB	
Single Rotor	750	57.5	0.2	55.8	0.3	1.7
	1000	62.0	0.3	60.1	0.7	1.9
	1250	64.7	0.2	64.0	0.5	0.7
Double $\theta = 0$	750	53.6	0.3	54.7	0.7	-1.1
	1000	61.0	0.5	58.3	0.3	2.8
	1250	66.2	0.6	63.2	0.5	3.0
Double $\theta = 15$	750	54.8	0.3	52.4	2.5	2.4
	1000	64.2	1.0	64.2	1.1	0.0
	1250	67.6	0.9	66.7	1.8	0.9
Double $\theta = 30$	750	51.5	1.4	51.7	3.7	-0.2
	1000	62.1	0.9	62.5	0.9	-0.4
	1250	67.5	0.8	66.9	0.9	0.6
Double $\theta = 45$	750	51.5	1.2	50.5	3.4	0.9
	1000	60.1	0.8	62.4	1.3	-2.4
	1250	67.5	0.7	65.9	0.4	1.7

Table A.1: Mean values (μ) and standard deviation (σ) of OASPL for Microphone #1 over $N = 5$ trial runs for the twisted blade rotor configuration at all azimuthal angles θ

Microphone #2 OASPL

Configuration	RPM	Baseline		Serrated		ΔOASPL
		μ, dB	σ, dB	μ, dB	σ, dB	
Single Rotor	750	56.9	0.4	55.0	0.5	1.9
	1000	63.8	0.2	62.3	0.2	1.5
	1250	66.8	0.4	66.2	0.4	0.6
Double $\theta = 0$	750	51.0	0.8	50.6	1.5	0.4
	1000	59.9	1.1	58.8	0.9	1.1
	1250	63.6	0.6	65.3	0.3	-1.7
Double $\theta = 15$	750	56.8	2.2	53.8	2.3	3.1
	1000	67.9	1.3	62.2	0.7	5.6
	1250	70.7	2.2	69.0	0.7	1.7
Double $\theta = 30$	750	51.2	1.5	56.6	3.1	-5.4
	1000	63.6	1.5	63.7	1.7	-0.1
	1250	64.5	1.5	67.4	0.3	-2.9
Double $\theta = 45$	750	51.8	0.7	50.0	2.9	1.8
	1000	61.2	1.3	62.0	2.1	-0.8
	1250	65.9	0.5	67.6	0.6	-1.7

Table A.2: Mean values (μ) and standard deviation (σ) of OASPL for Microphone #2 over $N = 5$ trial runs for the twisted blade rotor configuration at all azimuthal angles θ

Microphone #3 OASPL

Configuration	RPM	Baseline		Serrated		ΔOASPL
		μ, dB	σ, dB	μ, dB	σ, dB	
Single Rotor	750	59.0	0.6	57.5	0.4	1.4
	1000	65.8	0.4	65.0	0.3	0.8
	1250	69.8	0.4	68.4	0.4	1.4
Double $\theta = 0$	750	57.9	2.2	53.4	1.2	4.5
	1000	60.9	0.7	57.7	1.6	3.2
	1250	65.8	1.0	66.6	0.6	-0.7
Double $\theta = 15$	750	60.1	0.3	56.9	0.4	3.2
	1000	67.5	1.0	61.8	0.2	5.6
	1250	69.8	1.9	67.8	0.4	2.0
Double $\theta = 30$	750	54.9	1.5	54.3	1.5	0.7
	1000	63.6	1.1	62.3	0.6	1.3
	1250	65.1	0.6	65.4	0.9	-0.3
Double $\theta = 45$	750	55.2	0.6	52.6	0.3	2.6
	1000	59.5	1.5	63.0	1.5	-3.5
	1250	65.7	0.4	66.6	0.5	-0.9

Table A.3: Mean values (μ) and standard deviation (σ) of OASPL for Microphone #3 over $N = 5$ trial runs for the twisted blade rotor configuration at all azimuthal angles θ

Microphone #4 OASPL

Configuration	RPM	Baseline		Serrated		ΔOASPL
		μ, dB	σ, dB	μ, dB	σ, dB	
Single Rotor	750	57.5	0.3	55.4	0.1	2.1
	1000	63.6	0.5	62.9	0.1	0.8
	1250	67.1	0.2	67.2	0.1	-0.1
Double $\theta = 0$	750	53.4	0.2	52.6	0.2	0.8
	1000	60.2	0.4	58.2	0.3	2.0
	1250	64.6	0.3	63.5	0.3	1.1
Double $\theta = 15$	750	53.3	1.0	52.7	0.2	0.6
	1000	62.1	0.4	62.2	0.7	0.0
	1250	65.4	0.6	65.5	0.8	-0.1
Double $\theta = 30$	750	52.7	0.4	53.0	0.3	-0.2
	1000	61.6	0.2	61.9	0.1	-0.2
	1250	65.2	1.0	65.0	0.7	0.2
Double $\theta = 45$	750	53.8	0.7	53.8	0.3	0.0
	1000	61.0	0.5	63.1	0.6	-2.2
	1250	64.6	0.5	65.4	0.6	-0.8

Table A.4: Mean values (μ) and standard deviation (σ) of OASPL for Microphone #4 over $N = 5$ trial runs for the twisted blade rotor configuration at all azimuthal angles θ

Microphone #5 OASPL

Configuration	RPM	Baseline		Serrated		ΔOASPL
		μ, dB	σ, dB	μ, dB	σ, dB	
Single Rotor	750	59.2	0.2	57.3	0.4	1.9
	1000	65.5	0.4	63.2	0.3	2.3
	1250	68.5	0.4	67.6	0.3	0.9
Double $\theta = 0$	750	54.0	0.6	49.8	1.5	4.1
	1000	61.1	0.8	54.3	1.7	6.7
	1250	65.2	0.3	64.1	0.8	1.1
Double $\theta = 15$	750	55.5	1.2	55.5	1.2	0.0
	1000	67.7	2.3	62.4	1.0	5.3
	1250	64.9	1.0	63.3	2.6	1.7
Double $\theta = 30$	750	51.8	3.4	54.8	2.3	-3.0
	1000	66.1	1.9	62.8	1.4	3.3
	1250	61.8	1.9	67.5	0.8	-5.7
Double $\theta = 45$	750	58.8	3.6	53.0	0.9	5.8
	1000	67.6	2.8	58.1	2.8	9.5
	1250	61.8	1.8	68.4	0.9	-6.6

Table A.5: Mean values (μ) and standard deviation (σ) of OASPL for Microphone #5 over $N = 5$ trial runs for the twisted blade rotor configuration at all azimuthal angles θ

Microphone #6 OASPL

Configuration	RPM	Baseline		Serrated		ΔOASPL
		μ, dB	σ, dB	μ, dB	σ, dB	
Single Rotor	750	61.9	1.0	58.3	1.7	3.6
	1000	68.7	0.9	67.5	0.7	1.3
	1250	70.5	0.5	70.2	0.5	0.3
Double $\theta = 0$	750	56.9	1.7	55.0	1.4	1.9
	1000	65.0	1.4	62.3	1.5	2.7
	1250	70.5	1.7	66.9	3.5	3.6
Double $\theta = 15$	750	51.5	0.5	53.4	7.4	-1.9
	1000	62.8	9.7	66.4	6.3	-3.7
	1250	69.3	6.0	66.5	6.6	2.8
Double $\theta = 30$	750	57.1	6.1	62.0	1.2	-5.0
	1000	67.2	7.2	68.2	2.6	-0.9
	1250	70.6	6.9	68.6	6.6	2.0
Double $\theta = 45$	750	55.2	2.7	55.2	3.1	-0.1
	1000	67.6	9.9	65.1	7.1	2.5
	1250	74.5	6.1	73.1	2.9	1.4

Table A.6: Mean values (μ) and standard deviation (σ) of OASPL for Microphone #6 over $N = 5$ trial runs for the twisted blade rotor configuration at all azimuthal angles θ

Microphone #7 OASPL

Configuration	RPM	Baseline		Serrated		ΔOASPL
		μ, dB	σ, dB	μ, dB	σ, dB	
Single Rotor	750	57.5	2.0	57.9	1.5	-0.4
	1000	64.6	0.8	63.6	0.9	1.0
	1250	68.1	1.0	68.4	0.7	-0.3
Double $\theta = 0$	750	42.1	4.2	51.0	2.8	-8.9
	1000	50.7	5.7	54.8	4.1	-4.2
	1250	57.6	0.4	62.5	2.4	-4.9
Double $\theta = 15$	750	53.7	2.1	54.6	2.3	-0.9
	1000	62.4	3.2	59.8	1.2	2.6
	1250	63.3	3.9	67.0	3.0	-3.7
Double $\theta = 30$	750	49.7	5.7	49.4	4.9	0.3
	1000	59.4	0.6	58.4	0.5	0.9
	1250	55.0	5.1	60.1	4.6	-5.1
Double $\theta = 45$	750	49.5	6.0	53.6	1.4	-4.1
	1000	62.3	6.1	63.5	7.2	-1.2
	1250	64.5	3.2	62.1	5.1	2.3

Table A.7: Mean values (μ) and standard deviation (σ) of OASPL for Microphone #7 over $N = 5$ trial runs for the twisted blade rotor configuration at all azimuthal angles θ

Microphone #8 OASPL

Configuration	RPM	Baseline		Serrated		ΔOASPL
		μ, dB	σ, dB	μ, dB	σ, dB	
Single Rotor	750	53.1	1.0	57.3	1.0	-4.2
	1000	65.1	1.4	65.8	1.4	-0.7
	1250	68.5	2.0	68.1	2.1	0.4
Double $\theta = 0$	750	49.6	5.7	48.0	5.4	1.6
	1000	51.4	4.0	52.8	4.7	-1.5
	1250	62.3	5.7	64.3	3.4	-2.0
Double $\theta = 15$	750	54.0	1.5	52.2	5.5	1.8
	1000	61.4	2.2	56.2	2.1	5.2
	1250	68.3	1.3	66.2	1.2	2.1
Double $\theta = 30$	750	49.6	2.0	56.8	3.2	-7.2
	1000	58.9	5.2	56.7	1.0	2.2
	1250	62.0	3.0	67.3	1.9	-5.3
Double $\theta = 45$	750	55.9	3.6	56.4	2.9	-0.5
	1000	58.8	6.6	62.8	2.5	-4.0
	1250	58.3	2.1	63.2	1.9	-4.9

Table A.8: Mean values (μ) and standard deviation (σ) of OASPL for Microphone #8 over $N = 5$ trial runs for the twisted blade rotor configuration at all azimuthal angles θ

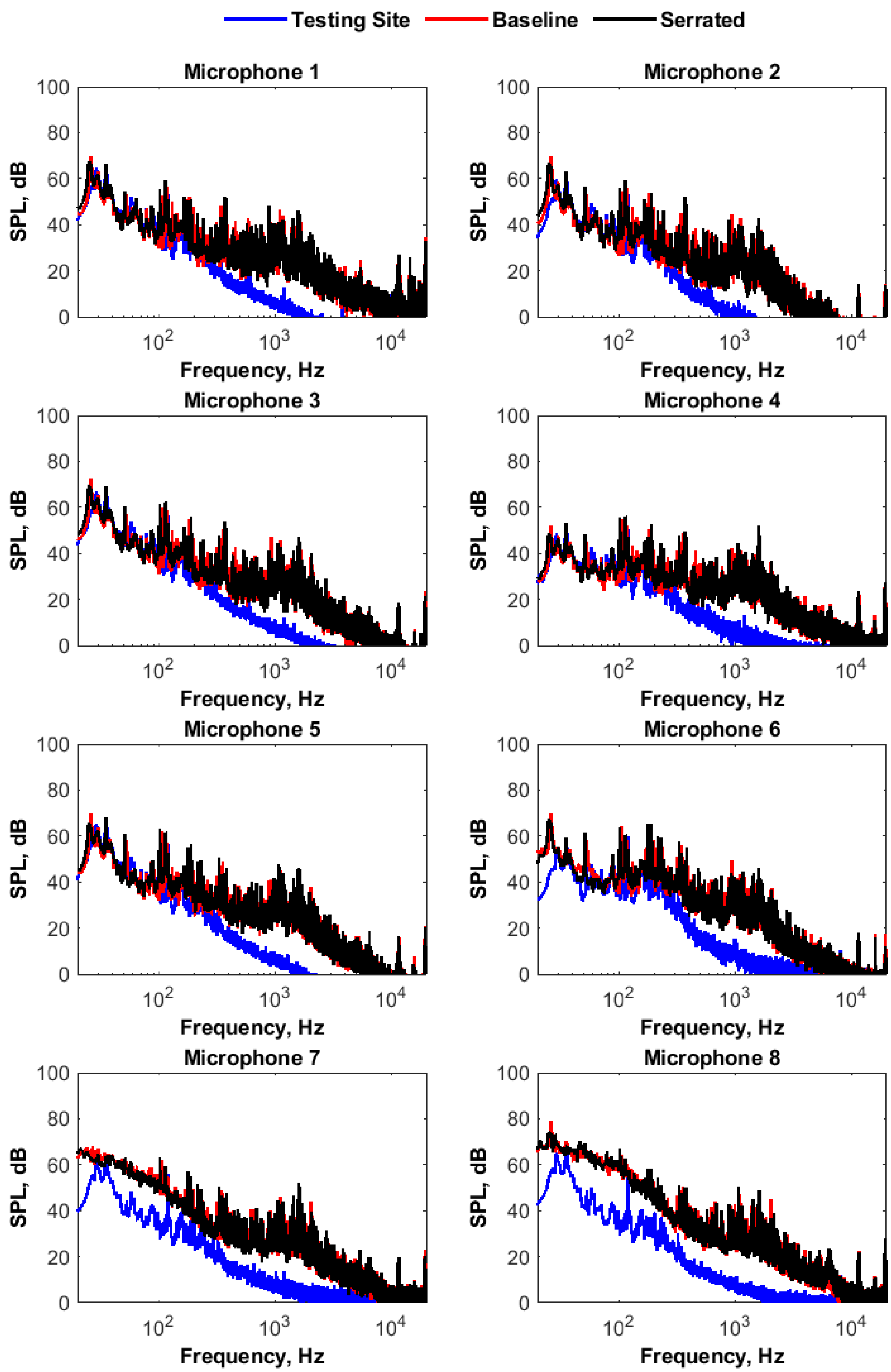

Figure A.1: Averaged Fourier Transform of acoustic signal from 20 to 20,000 Hz at 750 RPM

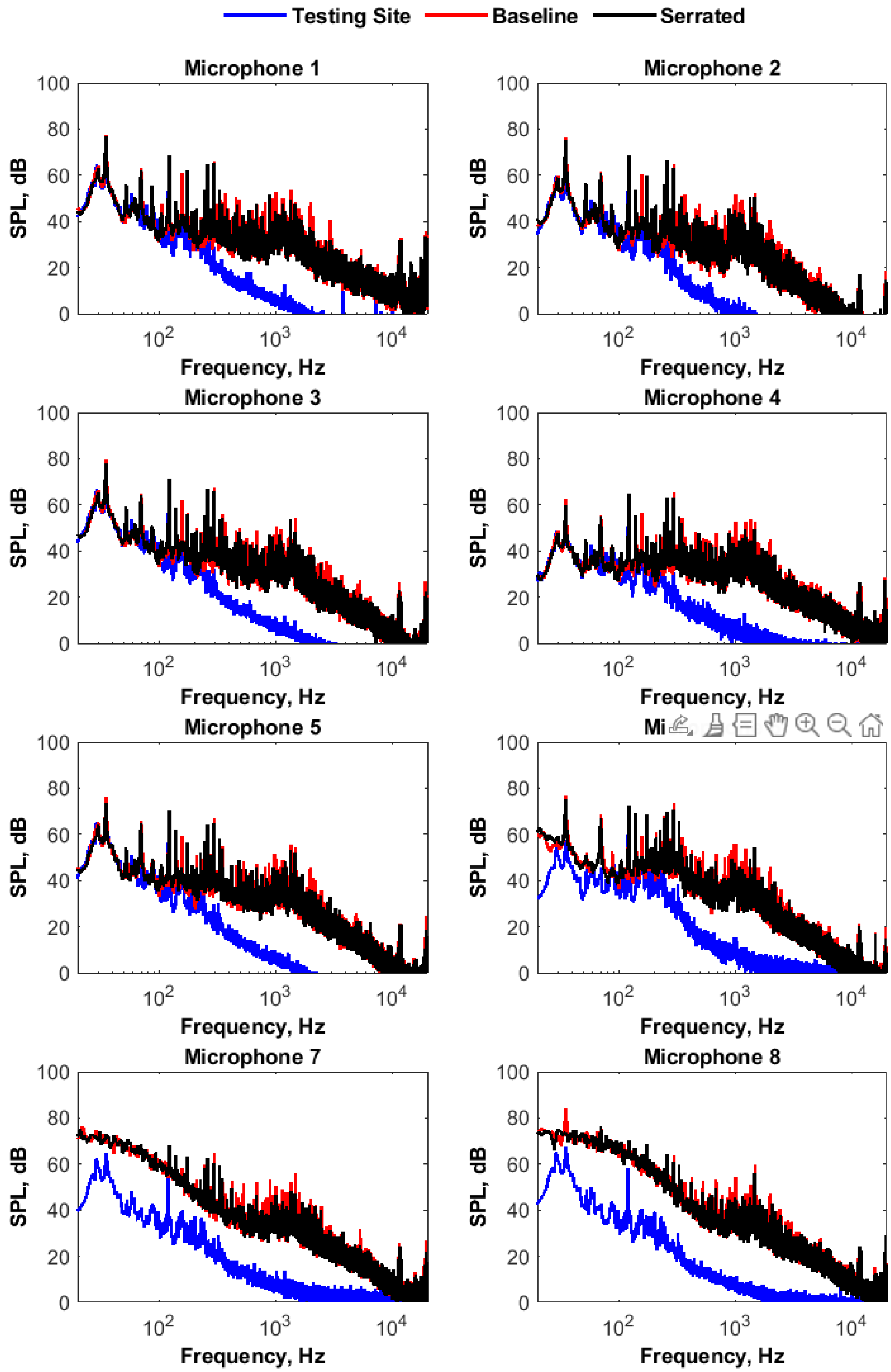

Figure A.2: Averaged Fourier Transform of acoustic signal from 20 to 20,000 Hz at 1000 RPM

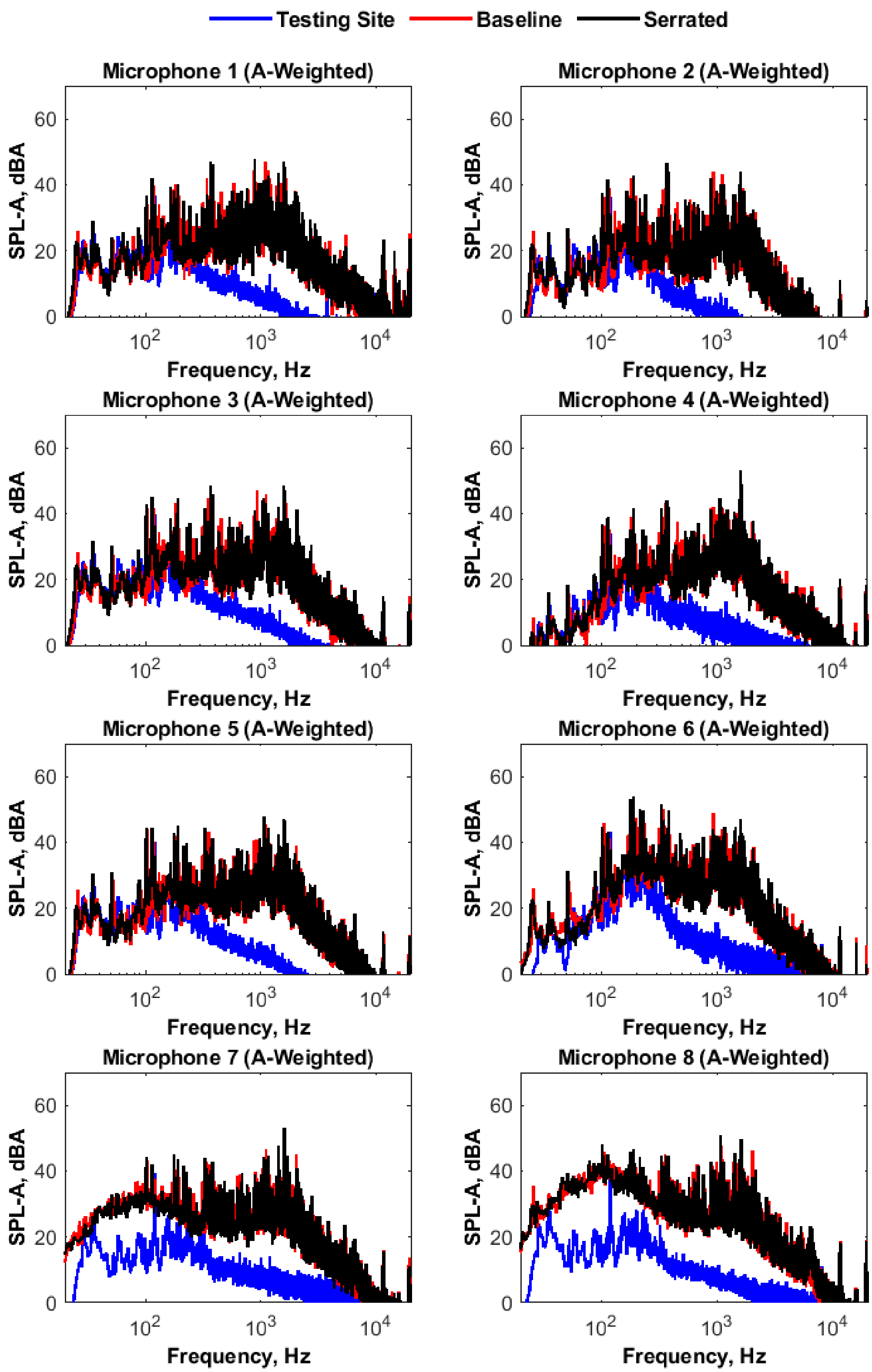

Figure A.3: Averaged Fourier Transform of acoustic signal from 10,000 to 20,000 Hz at 750 RPM

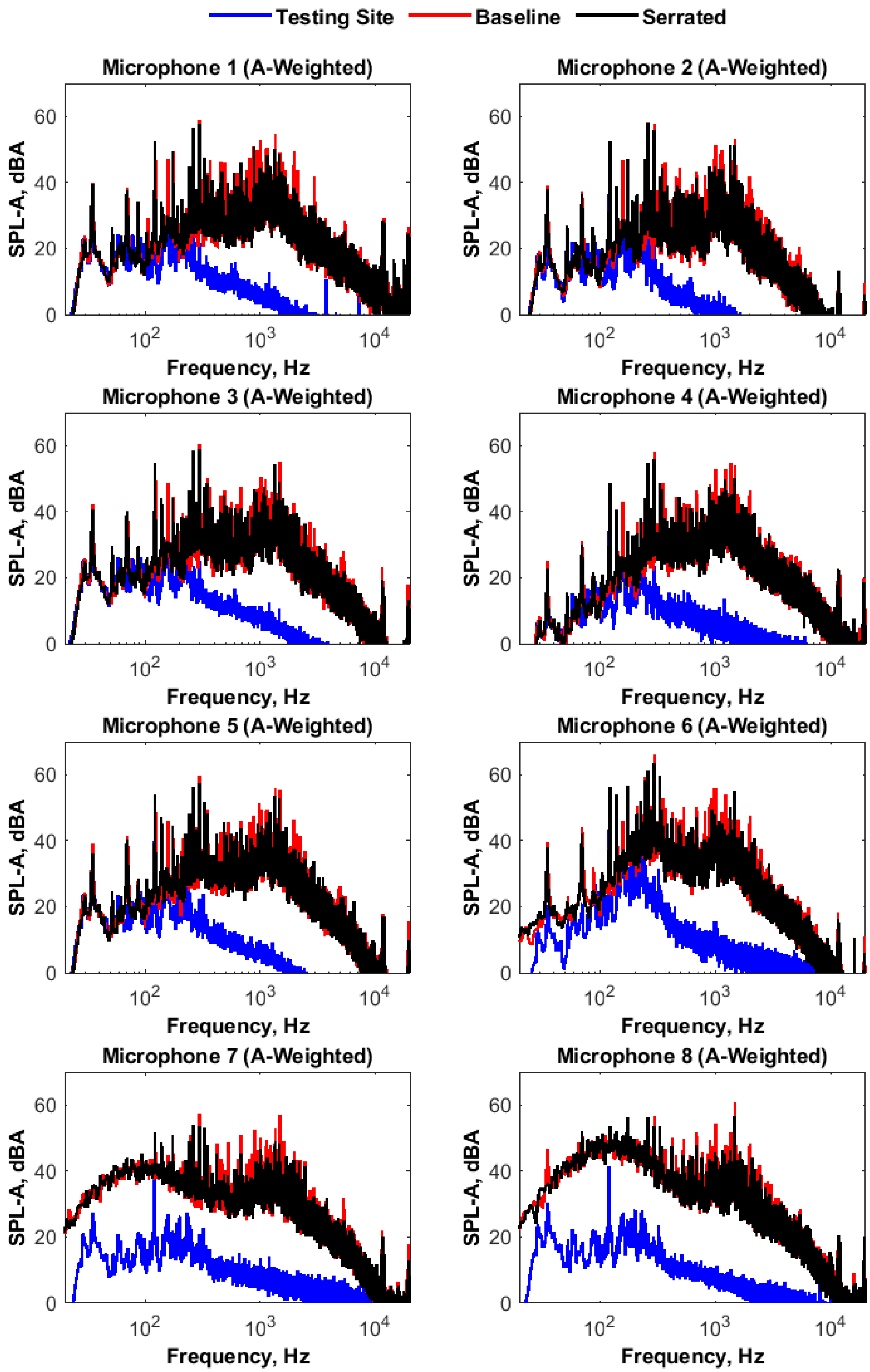

Figure A.4: Averaged Fourier Transform of acoustic signal from 10,000 to 20,000 Hz at 1000 RPM

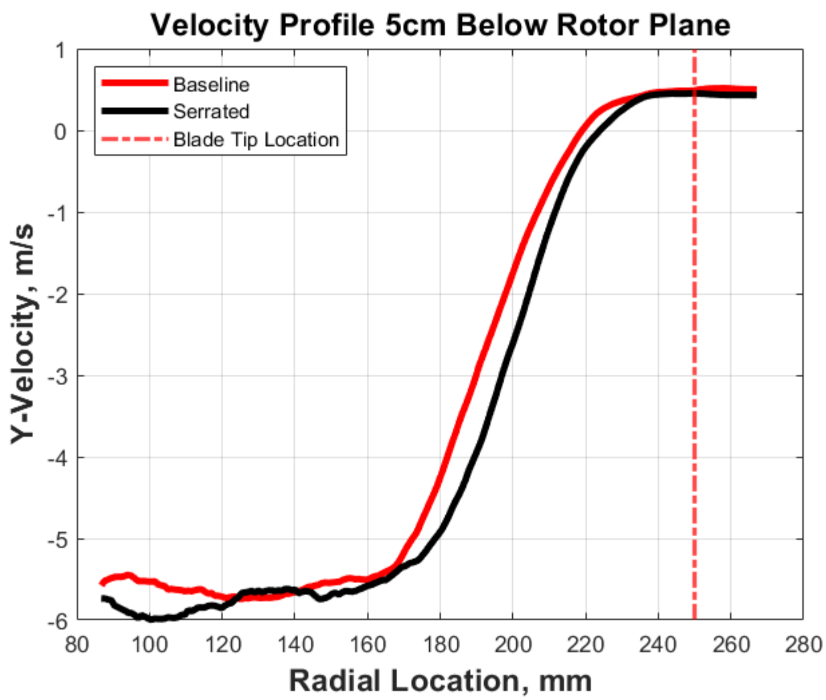

Figure A.5: Velocity profile 5 cm (0.10D) below the rotor plane for the baseline and serrated cases

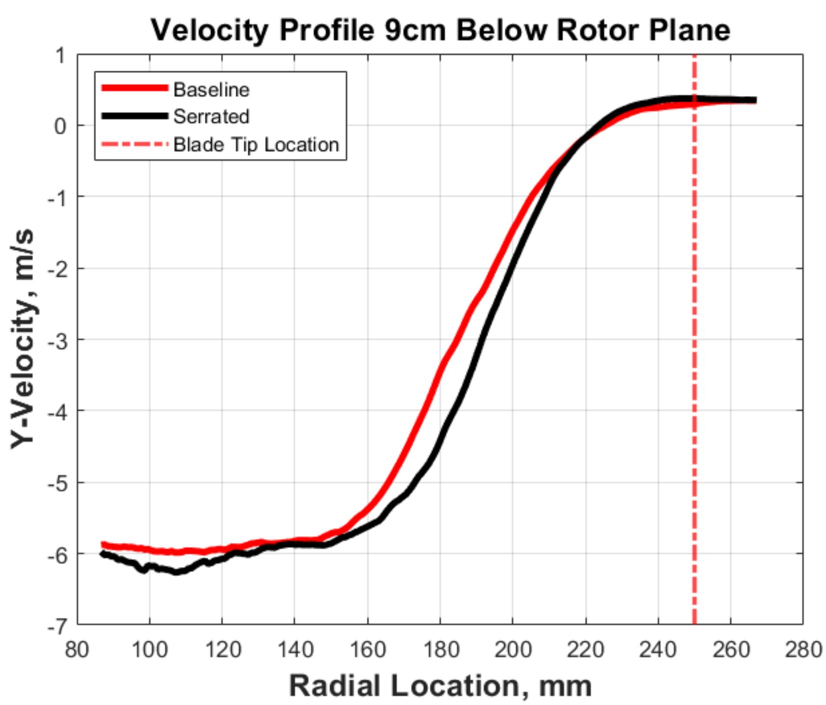

Figure A.6: Velocity profile 9 cm (0.18D) below the rotor plane for the baseline and serrated cases

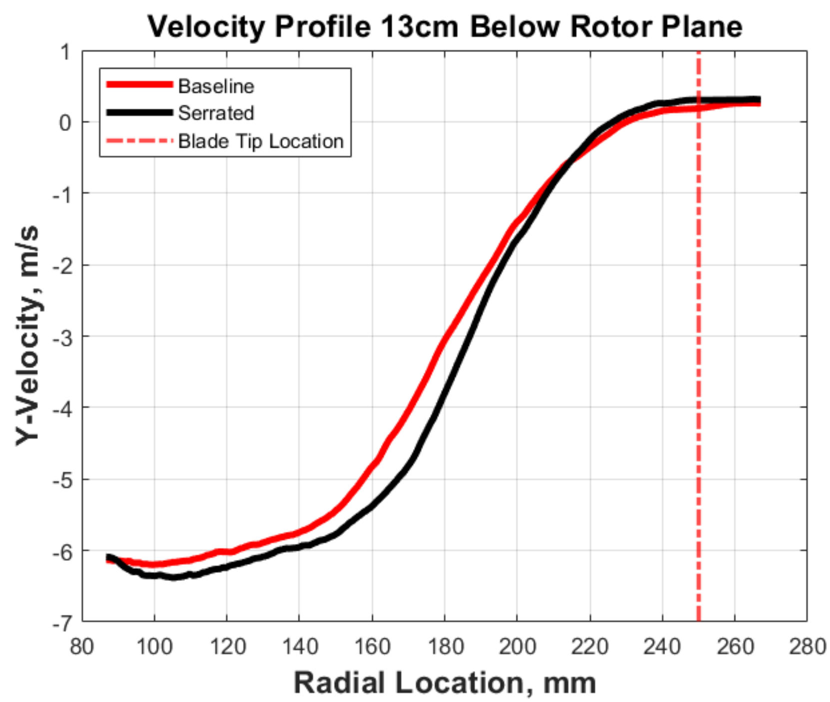

Figure A.7: Velocity profile 13 cm (0.26D) below the rotor plane for the baseline and serrated cases

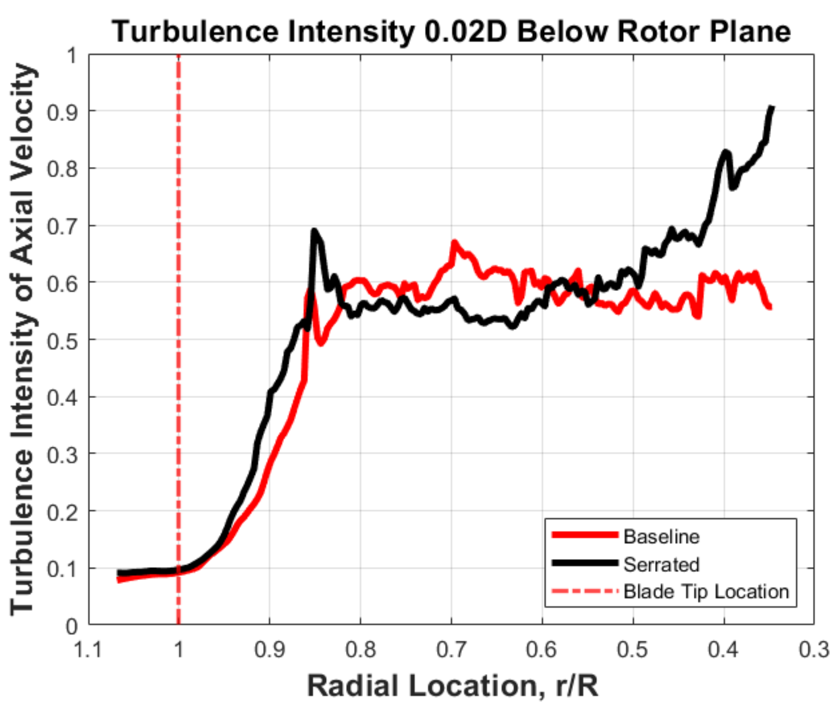

Figure A.8: Turbulence Intensity 1 cm (0.02D) below the rotor plane for the baseline and serrated cases

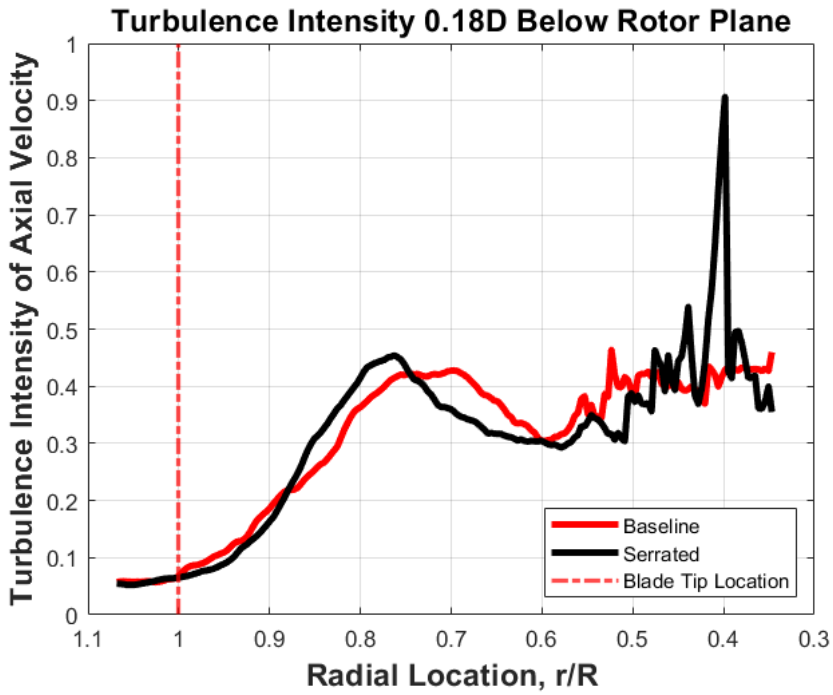

Figure A.9: Turbulence Intensity 9 cm (0.18D) below the rotor plane for the baseline and serrated cases

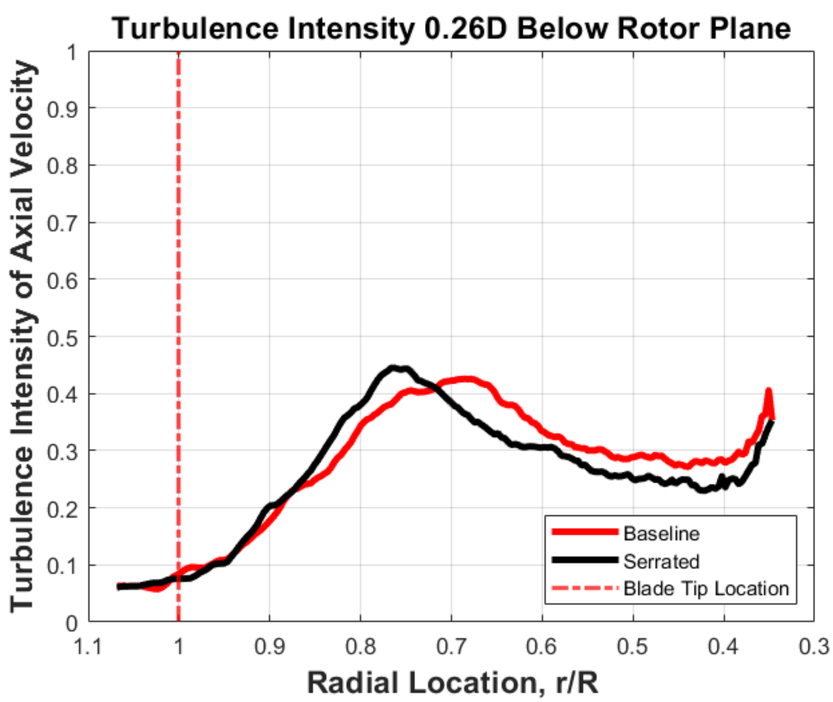

Figure A.10: Turbulence Intensity 13 cm (0.26D) below the rotor plane for the baseline and serrated cases